Investigation of AgCo Nanoparticles As a Useful Plasmonic Material

A Thesis Presented for the
Master of Science
Degree
The University of Tennessee, Knoxville

Vanessa Ramos

May 2013

Acknowledgments

I would like to thank my advisor, Dr. Ramki Kalyanaraman, for his tremendous support and guidance throughout this journey. I am also thankful for my lab mates who have served as resources of inspiration, guidance, and support: Sagar Yadavali, Abhinav Malasi, and Ritesh Sachan. Lastly, I would like to acknowledge the contributions from my collaborators and the financial support for this research:

- Ritesh Sachan for his contribution in obtaining the SEM images (S-4300, Hitachi and 40-FIB-SEM Crossbeam, Zeiss Auriga) 2.4.
- John Dunlap for allowing us to obtain images using his AFM (MFP 3D, Asylum Research) 3.8.
- Sustainable Energy Education and Research Center, Center for Materials Innovation, TN-SCORE, and NSF grants CMMI-0855949, DMR- 0856707, and ECCS-0850574.
- The Joint Institute of Advanced Materials (JIAM) at The University of Tennessee-Knoxville (UTK).
- Center for Materials Processing (CMP).

Abstract

Developing Localized Surface Plasmon Resonance (LSPR) sensors that are cost-effective, sensitive, and long lasting has been an important goal for those in the field of plasmonics. The starting point in creating improved sensors is finding the right materials that will overcome these major challenges. Presently Au and Ag are the most important LSPR metals because of their excellent plasmonic properties. However Au is expensive and has weaker plasmons than Ag, which suffers from environmental degradation. This thesis describes the investigations of a promising new plasmonic material, bimetallic AgCo, that can be used to solve some outstanding problems in LSPR sensing. The localized surface plasmon resonance (LSPR) characteristics of arrays of near hemispherical shaped AgCo nanoparticles (NPs) were investigated using broadband optical spectroscopy measurements. Arrays with varying NP size and composition were made by our collaborators using pulsed laser dewetting self-organization. The LSPR wavelength was significantly red-shifted from the value of pure Ag, consistent with predictions of effective medium models. The normalized bandwidth of the Ag-Co plasmons for compositions between 20 to 30% Co was comparable to that of pure Ag indicating the high quality of LSPR in this material. The sensitivity to detecting refractive index change was measured by immersion in liquids of various refractive index. The Ag-Co system showed comparable or better sensitivity than pure Ag NPs and was in the range of 50-100 nm/Refractive Index Units (RIU) for the range of size and composition studied. Another key result was the significantly improved stability of the LSPR wavelength and sensitivity values of the AgCo system as compared to Ag following storage of the samples for long times under ambient conditions or following annealing in air for 100 minutes at various temperatures. While pure Ag nanoparticles degraded substantially, the AgCo wavelength and sensitivity remained virtually unchanged. In total, these results showed that the AgCo system is substantially superior to pure Ag in many respects and could potentially replace Au and Ag as the materials of choice in future plasmonic applications.

Contents

1 Introduction **1**

1.1 History and definition of LSPR 1

1.1.1 Plasmon Dependence on Dielectric of Medium 2

1.1.2 Plasmon Dependence on Particle Diameter 3

1.2 Properties of LSPR 3

1.2.1 Wavelength location of LSPR 3

1.2.2 Bandwidth of the LSPR 5

1.2.2.1 Bandwidth from scattering effects 6

1.2.2.2 Bandwidth From interband transitions 6

1.2.2.3 *LSPR of Ag* 8

1.2.2.4 *LSPR of Co* 8

1.3 Principle of LSPR sensing 8

1.3.1 Sensing with Nanoparticles 9

1.4 Current challenges in LSPR sensing 11

1.5 Outline of Thesis 13

1.5.1 Outline 13

2 Experimental Procedures and Results **15**

2.1 Experimental Procedures 15

2.1.1 Sample Preparation 15

2.1.1.1 Thin Film Deposition and Irradiation 15

2.1.2 Processing 16

2.1.2.1 Annealing 16

2.1.3 Characterization 16

2.1.3.1 Optical Spectroscopy 16

2.2 Results 20

2.2.1 Absorption spectra as a function of composition and size 20

2.2.2 Absorption spectra as a function of medium refractive index 22

2.2.3 Absorption spectra as a function of time and temperature 22

3 Discussion **26**
3.1 Tunability of Wavelength 26
3.1.1 Bandwidth Dependence on Size and Composition 29
3.2 Sensitivity Dependence on Composition 31
3.3 Stability and Sensitivity Dependence on annealing conditions 32
3.3.1 LSPR following room temperature storage 32
3.3.2 LSPR and sensitivity following high temperature oxidation 34

4 Conclusions **38**
4.1 Summary 38
4.2 Future work 39

Bibliography **40**

Vita **44**

List of Tables

1.1 *Table above shows various sensitivity (nm/RIU) values for different Au nanostructures based on size and number of particles (single or array). Table taken from ref. [6].* 12

2.1 *The table below shows the various combinations of nanoparticles made with this synthesis technique.* 17
2.2 *Film thickness ratios listed along with the particle diameters.* 17
2.3 *Mediums used for optical experiments.* 17
2.4 *The extracted LSPR values from the absorbance spectra of different Ag compositions are listed below.* 23

3.1 *Bandwidth values of the absorbance spectra as a function of composition for different particle sizes.* 30
3.2 *Sensitivity values calculated from the slopes of the curves.* 33

List of Figures

1.1 *Localized surface plasmons caused by net displacement of free conductive electrons in nanoparticle. Figure taken from ref. [3].* 4

1.2 *(a) The real part of the dielectric of various metals. The location of the LSPR is at the intersection point of the metal dielectric with -2 times that of the surrounding dielectric. For example, ,intersection with a red horizontal line at -2 will signify plasmon resonances in air. As seen here, Ag, Au, and Na have visible wavelength LSPRs. In comparing the noble metals (Ag and Au) with the Alkali metals (Na and K), the rate of change of the dielectric function (slope) is smaller for the noble metal curves, and this results in higher sensitivity to detecting changes in surrounding dielectric. (b) The imaginary component of the dielectric of the various metals. This determines the quality of the plasmon peak. Ag has one of the lowest electron losses within the visible range, even less then Au, and is comparable to the alkali metals. The collective effects from the dielectric function, show Ag to be the material with the best plasmon in the visible range. Figures taken from [12].* 4

1.3 *(a) Au spherical nanoparticles show bandwidth increases with increasing particle diameter, when the diameters are > 20 nm. Figure taken from [10]. (b) The absorption coefficient of Ag when particle diameters are < 20 nm. The peak broadens as the particle diameter decreases, confirming a 1/R relationship in this region. Figure taken from [15].* 7

1.4 *(a) The real parts of the dielectric function (ε') for Ag (solid line) and Co (dashed line) as a function of energy. The intersection of the dielectric functions with the air line ($\varepsilon' = -2$) and SiO_2 line ($\varepsilon' = -4.9$) is also shown. At these intersections the metals will show plasmon resonances in the respective host medium. Figure taken from [16]. (b) The real part of the Ag dielectric showing the contribution from interband transitions and the Drude contribution. Figure taken from [17]. (c) Absorption coefficient for Ag and Co nanoparticles embedded in SiO_2 host matrix with a volume fraction of 5%. It can be seen that the LSPR for Co is completely suppressed because of its proximity to the Co interband transition of 3.8 eV. However the Ag LSPR is extremely sharp. Figure taken from [16].* 7

1.5 *SPR vs LSPR sensing. (a) In SPR sensing, shift in plasmonic wavelength of $\Delta\lambda_P$ at the total internal reflection angle of the prism - metal interface (Kretschmann geometry), corresponding to SPR excitation, is measured and correlated with change in refractive index n due to chemical interactions on the metal surface. (b) In LSPR sensing, the relative change in reflectivity R_p at the LSPR resonance. The increased sensitivity of NP to change in n is due to the ability to differentiate small changes in R_p with chemical changes [23]. This increased sensitivity for NP is shown in the center panel as the trend line with larger slope for the behavior of measured signal versus n.* 10

1.6 *(a) Scattered light of Ag nanoparticles as refractive index of liquid is changed, from air (n=1.00) to various oils (starting from n=1.44). (b) Sensitivity plots derived from normalized spectra in (a). The peak positions are maxima of extinction spectra at specific wavelengths, on the y-axis. The indices of the oil are plotted on the x-axis. The slope from these plots constitutes the sensitivity of the measurements in units of nm/RIU. Figures taken from [24].* 10

1.7 *The figure above shows the various materials and their plasmonic maximum QLSP which describes the maximum quality of the surface plasmon resonance. It is shown that Co has a low plasmon quality while Ag has a high quality plasmon, comparable to Au and Cu. Figure taken from ref. [11].* 12

2.1 *Optical set-up for the sensitivity and oxidation experiments. The UV-Vis light source is connected to an optical fiber that transmits its light to the sample on the platform (area inside the green rectangle). The optical fiber serving as the detector is attached underneath the platform and this is connected to the spectrometer on the table. The spectrometer collects this transmission data and sends it to the computer via a usb cord. The data is then output into the Ocean Optics Spectra Suite software.* 18

2.2 *Screenshot of Spectra Suite software showing reference spectrum on quartz substrate.* . . . 18

2.3 *(a) The container which was used to contain the different liquids during sensitivity experiments. A quartz substrate for the reference was placed inside as shown and the sample alongside it. (b) The optical fiber probe is lowered into the container as close as possible so the maximum transmission intensity can be obtained.* 19

2.4 *SEM images taken for different Ag % compositions: (a) 100 % Ag (b) 83 % Ag-17% Co (c) 72% Ag-28% Co. Size histograms show a narrow distribution.* 21

2.5 *Raw (unnormalized) absorption spectra for samples with varying Ag % composition (a) 100% Ag (b) 83.3% Ag-17% Co (c) 72% Ag-28% Co. In each figure, the spectra for arrays with different average particle diameter is also shown where the bandwidth difference between compositions is more noticeable.Normalized absorption spectra from samples with varying Ag % composition (d) 100% Ag (e) 83.3% Ag-17% Co Ag (f) 72% Ag-28% Co. In each figure, the spectra for arrays with different average particle diameter is also shown* . . . 21

2.6 *Raw spectra of sensitivity measurements for 90 nm particles with different Ag % compositions: (a) 100% Ag (b) 83% Ag-17% Co (c) 72% Ag-28% Co. There is an obvious red shift trend seen as the refractive index of the liquid is increased, from air to glycerol. This behavior follows the Mie theory. Normalized sensitivity spectra of 90 nm particles for different compositions: (d) 100% Ag (e) 83% Ag-17% Co (f) 72% Ag-28% Co* 23

2.7 *Raw Absorbance spectra of (a) Ag with 56 nm average diameter and (b) AgCo (83% Ag-17% Co) with 85 nm average diameter, for various days following storage in ambient air at room temperature. Normalized spectra shown in (c) 100% Ag with 56 nm average diameter and (d) 83% Ag-17% Co with 85 nm average diameter.* 24

2.8 *(a) Raw absorbance spectra of a Ag sample annealed for 100 minutes at various temperatures. There is a general blue shift of the LSPR that can be seen in this data as well as the decay of the plasmon. (b) Similar spectra for AgCo annealed at 100 minutes for same temperatures. The LSPR here is not shifting throughout the annealing process. (c) Normalized absorbance spectra of Ag annealed at 100 minutes for different temperatures. The shift in the LSPR becomes clearer when the spectra are normalized. There is indeed a blue shift in the LSPR for Ag. (d) For the normalized AgCo (83% Ag-17% Co) spectra, the LSPR is not changing.* 25

3.1 *(a) Experimentally measured LSPR shift (symbols) with varying Ag % for arrays with different average particle diameters. The position of the LSPR was obtained from the absorbance curves in Ch 2. (b) Experimentally measured LSPR shift (symbols) with varying particle size for various Ag %. The trend lines in both figures are results of effective medium modeling. The figures were taken from ref.* [34]. 28

3.2 *The schematic model to estimate the effective dielectric function of the AgCo nanoparticle array layer formed by hemispherical particles of radius h on top of a SiO_2 substrate. The Ag and Co grains were assumed to be randomly distributed in the nanoparticle. The figure was taken from ref.* [1]. 28

3.3 *Experimentally extracted data for LSPR bandwidth normalized by the LSPR position as a function of Ag % (a) and particle size (b). On the y-axis is Bandwidth/LSPR peak ($\triangle\lambda/\lambda_{LSPR}$). The various lines are guides to the eye.* 30

3.4 *LSPR wavelength change versus refractive index for the various Ag and AgCo systems for two different particle sizes. The filled symbols (solid lines) correspond to 90 nm particles and the open symbols (dashed lines) correspond with 110 nm particles. Figure taken from [34].* 33

3.5 *(a) Schematic illustration of the role of size on LSPR sensing. Hemispherical nanoparticles of diameter D are arranged on a surface with spacing Λ. The localized plasmon decay length around each particle is δ and determines the region within which refractive index changes can be measured. (b) Plot of the experimentally measured sensitivity S vs. D_{eff}^2/Λ^2 for ther various Ag and AgCo arrays investigated.* 34

3.6 *(a) LSPR wavelength versus number of days at room temperature for Ag (open symbols) and AgCo (closed symbols) (b) Normalized inverse bandwidth of the LSPR peak as a function if time at room temperature for Ag (closed symbols, solid line) and AgCo (open symbols, dashed line). Symbols are experimental data while the lines are fits to the behavior. Fig. (b) was taken from ref. [42].* 35

3.7 (a) λ_{LSPR} following heating of the arrays in air at various temperatures for 100 minutes. AgCo data is shown by the closed square symbols while Ag corresponds to the open round symbols. (b) *Sensitivity of LSPR detection for arrays of pure Ag (open round symbols, dashed blue line is guide for the eye) and AgCo (closed square symbols, solid red line is horizontal guide line for the eye) for samples subjected to heating at various temperatures for 100 minutes.* 35

3.8 *(a) Atomic force microscopy (AFM) image of a freshly prepared Ag nanoparticle array. This data was used to analyze the average peak to valley height of the NPs, which is a useful measure of the average height of the particles. (b) AFM of the Ag NP array shown in (a) but after its heating in air at 100ºC for 100 minutes.* 37

Chapter 1

Introduction

The research presented in this thesis is focused on investigating the localized plasmonic properties of bimetallic nanoparticles made from Silver (Ag) and Cobalt (Co). Specifically, since this material has only recently been shown to have interesting localized surface plasmonic resonance (LSPR) behavior [1], the objective here is to quantitatively establish the efficacy of using these materials in chemical sensing applications based on the principle of LSPR sensing. Therefore, we begin this thesis by first providing a detailed background discussion of the LSPR as well as LSPR sensing. Following this, we review the challenges faced by currently available metals in their use as LSPR materials and overview the promise of the AgCo system. The experimental results and the observations supporting the advantages of AgCo will be discussed throughout the remainder of the thesis. A brief summary and a look into the future work of LSPR sensing will be mentioned in the closing remarks.

1.1 History and definition of LSPR

The interaction between optics and materials has helped plasmonics grow over the years, by developing chemical sensing applications [2, 3, 4, 5]. Before delving into the experimental portion of this thesis, it is necessary that the background and theory behind Localized Surface Plasmon Resonance (LSPR) be explained. In short, LSPR is caused by the collective oscillations of free conductive electrons inside a metal particle, which is in turn caused by the interaction with incident energy, such as electromagnetic (EM) energy. Although Michael Faraday was the first to describe the effects of gold particle size on the perceived color change, Gustav Mie described this phenomena using theory to confirm these experimental observations [6, 7, 8]. Influenced by Faraday's work, he performed similar experiments and discovered what effects light scattering and particle size have on the visible color of gold nanoparticles. Today, we are able to understand the reasoning behind this phenomena based on the electron excitations that occur under incident light. As light hits the metal particle, the electric field component of that light causes a net displacement of the free conductive electrons so that a net dipole moment is produced. The electric field due to the polarization, causes a restoring force which gives rise to the oscillation of free electrons inside a metal. These oscillations create a plasmon frequency and the plasmons are in resonance when the frequency of the light matches that of the oscillations. The plasmons are considered localized, because they are confined to the nanoparticle

space, as shown in Figure 1.1 [3, 6, 5, 4].

Mie observed the color of gold nanoparticles changed to red, as the particle diameter increased. From this study, he was able to find that the light scattering behavior in the particle, correlates with the physical concept of resonance, eventually giving rise to the field of plasmon sensing, as we know it today. The wavelength dependence of light scattering behavior on the dielectric function is best shown by the equation described in the Mie Theory [6]:

$$\sigma_{ext} = \frac{18\pi\varepsilon_h^{3/2}V}{\lambda}\frac{\varepsilon_m''(\lambda)}{[\varepsilon_m'(\lambda)+\chi\varepsilon_h]^2+\varepsilon_m'(\lambda)^2} \tag{1.1}$$

The real and imaginary dielectric components for the material, ε_m' and ε_m'', and that of the dielectric medium, ε_h, affect the light being absorbed or scattered, which will ultimately change the extinction cross-section. Here V and λ correspond to the volume of the particle and the wavelength of light respectively. Although the extinction cross section σ_{ext}, describes the absorption and scattering cross-sections, this equation has been widely used to explain the absorption spectrum and the condition under which an LSPR peak is observed. If the equation is further reduced to,

$$\sigma_{ext} = C\frac{\varepsilon_m''(\lambda)}{[\varepsilon_m'(\lambda)+\chi\varepsilon_h]^2+\varepsilon_m'(\lambda)^2} \tag{1.2}$$

where C is a constant that encompasses the $\frac{18\pi\varepsilon_h^{\frac{3}{2}}V}{\lambda}$term in the Equation 1.1, the condition needed to maximize the spectrum becomes apparent by minimizing the denominator. In order for this to happen, the first squared term must be set to 0. The χ term is a geometrical parameter related to the shape of the particle. Since Mie was dealing with spherical particles, for which χ has the value 2, one obtains the well known condition of a plasmon resonance at the metal surface to be $\varepsilon_m'(\lambda) = -2\varepsilon_h(\lambda)$.

1.1.1 Plasmon Dependence on Dielectric of Medium

The important relationships to consider, can be extracted from Equation 1.2. By looking at the dielectric condition, it is obvious the real part of the material dielectric function determines the maximum absorption wavelength of the particle. Furthermore, the dielectric of the medium also plays a huge role in determining the resonance absorption. Since the refractive index n of the dielectric is related to is dielectric function by $\varepsilon_h = n^2$, so changes in the surrounding refractive index, such as by varying the medium, will greatly affect the wavelength position of the plasmon resonance.

Additionally, the imaginary component of the material dielectric function also plays a role in the plasmon resonance, in terms of damping. The damping of the electron oscillations are analogous to the damping that occurs in a mechanical system. As the damping reduces the amplitude of the electron oscillations, this causes broadening in the absorption resonance peak and a decrease in the intensity of the absorption. Known as radiative damping or decay, this effect is explained further when discussing the size dependence of the plasmon [3, 5, 4, 6].

1.1.2 Plasmon Dependence on Particle Diameter

While equation 1.1 is generally true for nanoparticles over a wide size range, there are different factors that contribute to a size-dependent behavior, which leads to a shift and decay of the plasmon. Two behaviors exist depending on the following relationship between the diameter and the light wavelength. When particles are $2R \ll \lambda$, where R is the radius of the particle, the absorption dominates over scattering in the LSPR extinction because the dipole oscillation is substantially contributing to the plasmon. However, when particles become comparable to the wavelength, the light can no longer polarize the particle homogeneously and scattering dominates. Here radiative decay is primarily responsible for the decay of the plasmon oscillations, causing the absorption resonance to have a lower intensity and a broader peak, as we discuss in Sec. 1.2.2. During this stage, the particle can also have quadrupole or higher-order oscillation modes. Since these higher-order modes occur at lower frequencies, the LSPR plasmon can also red-shift towards longer wavelengths [9, 10, 4].

1.2 Properties of LSPR

In evaluating the possible materials that could be used in plasmonic applications, there are some general features of relevance, for example the wavelength location of the LSPR, the sharpness (bandwidth) of the LSPR, how it responds to changes in the external environment, and the long term stability of the material itself. As we show, based on these general characteristics, there are a very limited choice of materials available for plasmonic applications in the visible optical range. Specifically it can be shown that visible localized surface plasmons primarily occur in nanoparticles of noble metals (Ag, Au and Cu) and alkali metals (Na, K), while most other metals, including the ferromagnetic elements, have non-existent visible plasmons [11, 12].

1.2.1 Wavelength location of LSPR

As discussed in Sec. 1.1, Mie's theory provides a simple condition, $\varepsilon'_m(\lambda) = -2\varepsilon_h(\lambda)$, for the existence of the plasmon resonance. Since all metals have a unique wavelength dependent dielectric function, the LSPR wavelength of different metals can be expected to differ. Indeed, if one evaluates some common metals a large difference in their LSPR wavelength can be seen if one takes a look at the real and imaginary dielectric components versus wavelength, as shown in Figure 1.2.

The real part of the dielectric function indicates the sensitivity and LSPR wavelength for various metals. In the above figure (Fig. 1.2), the noble metals possess a plasmon when the Mie condition is met, for example, when the real part will equal to -2 when the dielectric of the medium is air (ε_{air}=1). As can be seen, the wavelengths are within the visible range at this stage. The imaginary component, however, indicates the quality of the plasmon peak. The low numbers in Ag and alkali metals suggest smaller electron scattering rates and hence lower rate of loss in the visible regime due to processes such as scattering and interband transitions. It is important to note, although Au has larger ε'' values than Ag in the visible wavelengths, it still exhibits its lowest loss in this range. Taking into account the ε' values, the noble metals have best

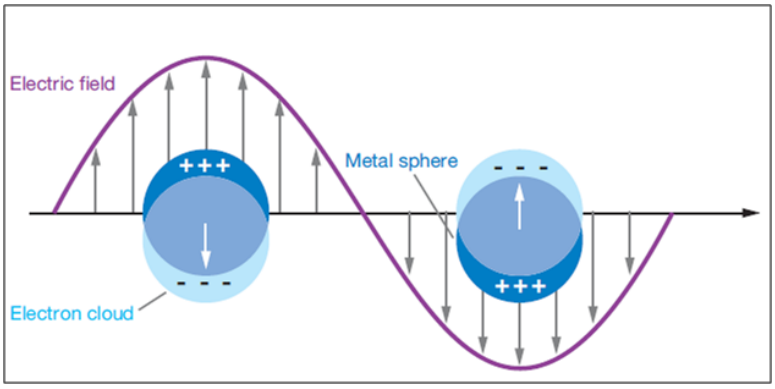
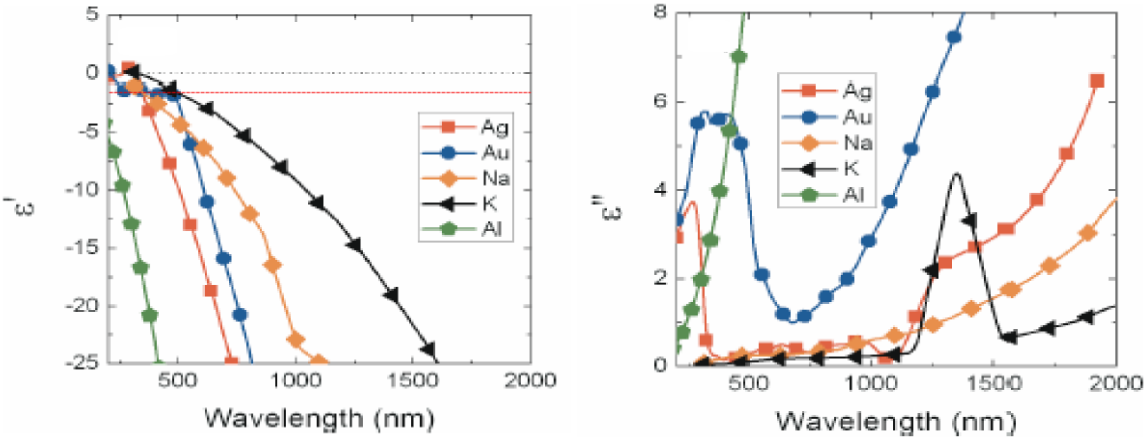


Figure 1.1: *Localized surface plasmons caused by net displacement of free conductive electrons in nanoparticle. Figure taken from ref. [3].*



(a) (b)

Figure 1.2: *(a) The real part of the dielectric of various metals. The location of the LSPR is at the intersection point of the metal dielectric with -2 times that of the surrounding dielectric. For example, ,intersection with a red horizontal line at -2 will signify plasmon resonances in air. As seen here, Ag, Au, and Na have visible wavelength LSPRs. In comparing the noble metals (Ag and Au) with the Alkali metals (Na and K), the rate of change of the dielectric function (slope) is smaller for the noble metal curves, and this results in higher sensitivity to detecting changes in surrounding dielectric. (b) The imaginary component of the dielectric of the various metals. This determines the quality of the plasmon peak. Ag has one of the lowest electron losses within the visible range, even less then Au, and is comparable to the alkali metals. The collective effects from the dielectric function, show Ag to be the material with the best plasmon in the visible range. Figures taken from [12].*

plasmons, and Ag is the best known plasmonic metal. The LSPR wavelength shift arising from changes in the surrounding dielectric, is the underlying principle of LSPR sensing, which we discuss in more detail in Sec. 1.3.

1.2.2 Bandwidth of the LSPR

Another practically relevant characteristic of the LSPR is the sharpness of the peak, also known as the bandwidth and is measured by the full-width-half-maximum (FWHM). The width of the peak is determined by first normalizing the absorption peak and then finding the width at 1/2 the maximum intensity of the spectrum. The narrowness or broadness of the spectrum directly determines the quality of the plasmon and what is happening to the electron oscillations. In fact, the bandwidth is a fundamental indication of the behavior of the electrons in a metal. As we will discuss in this section, the spatial bandwidth $\Delta\lambda_{LSPR}$ often determines the ultimate usefulness of a metal in plasmonic applications. In fact, this is one of the primary reasons why Ag is the most important plasmonic metal, as discussed here. For a free electron gas the dielectric function in the Drude-Lorentz-Sommerfield model can be expressed as the permittivity of the material, $\varepsilon_m(\omega)$ [13]:

$$\varepsilon_m(\omega) = 1 - \frac{\omega_p^2}{\omega^2 + i\gamma\omega} \tag{1.3}$$

The bulk plasmon frequency, $\omega_p^2 = ne^2/\varepsilon_o m^*$, is determined by the electron density n, the electron effective mass m^*, the electron charge e, and the permittivity of vacuum ε_o. The damping constant γ determines the rate at which the plasmon dephases, i.e. the electrons in the collective oscillation lose coherence, which is responsible for the reduction in intensity and broadening of the plasmon peak. This term is equal to the bandwidth in the visible spectrum regime, $\gamma << \omega$. In this regime, a free electron gas is assumed [10, 13]. The contributing factors to the bandwidth may be divided into intrinsic and extrinsic parts. The intrinsic part is a material specific property that arises from various electron scattering processes.

The total dephasing rate can be expressed via Mathiessen's rule as the sum of the reciprocal of all relaxation times τ that includes electron-electron, electron-phonon, electron-defect, and electron-surface scattering processes. Inelastic scatterings result in intra- and inter-band transitions, which contribute to plasmon energy loss. An alternate view of the decay of plasmons is based on an analogy with molecular spectroscopy. As shown by Heilweil et. al. and Link and El-Sayed [10, 14], the interaction of incident EM waves with the free electrons can be interpreted as excitations in a two-level system and subsequent decay via radiative and non-radiative transitions. In this model, the total dephasing time T_2 is expressed as

$$\frac{1}{T_2} = \frac{\Delta\omega_{LSPR}}{2} = \frac{1}{2T_1} + \frac{1}{T_2^*} \tag{1.4}$$

where $\Delta\omega_{LSPR}$ is the frequency bandwidth of the LSPR, also known as the temporal bandwidth, T_2^* is the dephasing time due to elastic scattering processes, and T_1 is the energy (population) relaxation time via radiative and non-radiative processes. It was proposed by Kriebig, that the electron scattering is enhanced in smaller particles due to a smaller electron mean free path. As we will see, the bandwidth is influenced by interband transitions, but also by particle diameter, when the diameter is < 20 nm. For diameters > 20 nm,

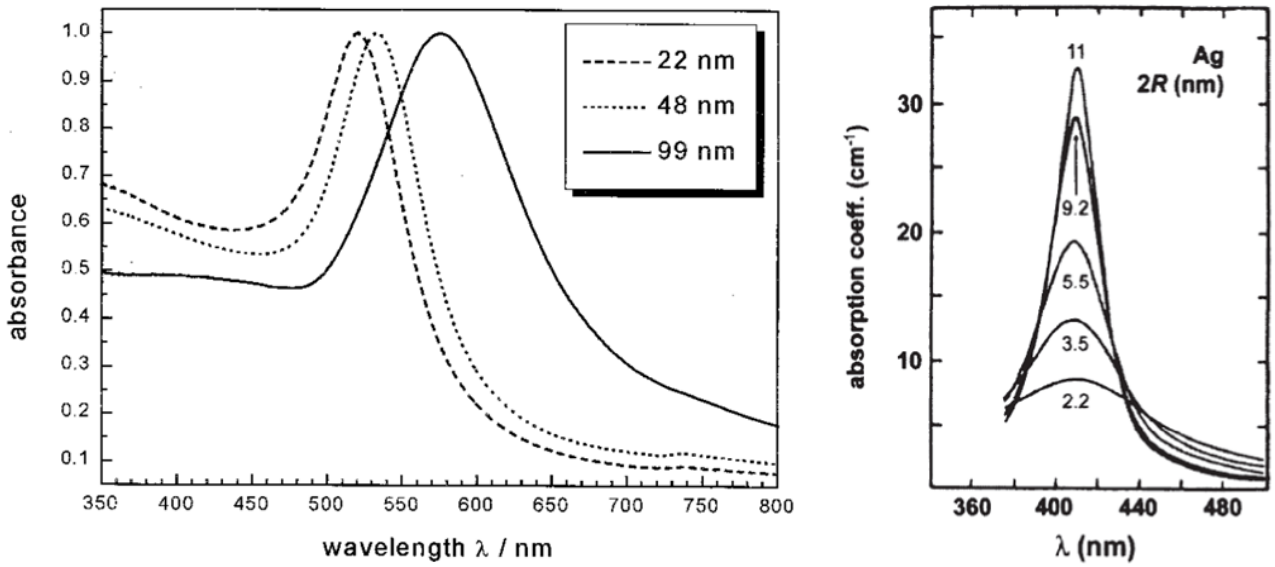
the bandwidth increases.

1.2.2.1 Bandwidth from scattering effects

As discussed in Sec. 1.1.2, the bandwidth increases as the particle diameter increases. Yet this is only for a large particle diameter 20 nm. Notice in Fig. 1.3(a), the bandwidth is increasing as particle diameter increases, but also red shifts. This is following the fundamental Mie Theory where it is expected to red-shift because of the influence of higher order modes. At the same time, due to the elastic scattering effects, such as from electron-electron collisions, the bandwidth is expected to increase. As depicted in Figure 1.3(b), the bandwidth relationship changes when particles are < 20 nm. As Kriebig realized, the scattering is enhanced in small particles because of the electron mean free path. If the particle diameter is less than the mean free path of an electron, the electron reaches the surface quicker and hence scatters quicker. These are electron-surface collisions, otherwise known as inelastic scattering effects, which cause the electrons to lose coherence more quickly. Therefore, in the small size regime, the plasmon wavelength is not affected, but the bandwidth increases greatly with decreasing size [10, 9].

1.2.2.2 Bandwidth From interband transitions

Based on the relative magnitudes of the elastic and energy relaxation times, one can characterize the behavior of different metals. Here we specifically show the difference between the best plasmonic metal, i.e. Ag and a weak one, i.e. Co. Fig. 1.4(a), shows the difference in the dielectric dispersion between Ag and Co when glass or air is used as a medium. It is clear that for Ag there is a smaller difference in the LSPR energy between the two different mediums. In the case of Co, the energy change for resonance between glass and air is larger, denoted by the lower slope. In Fig. 1.4(b) the Ag dielectric function is broken up into contributions from the Drude model and interband transitions, and large interband transitions are evident in the UV energy regime of ~4 eV. In Fig. 1.4(c), the LSPR of Ag and Co are compared and clearly demonstrates the much larger intensity of Ag plasmons at the Mie condition as compared to Co. The interband transitions are playing an important role in suppressing the Co LSPR, as discussed subsequently.



(a) (b)

Figure 1.3: *(a) Au spherical nanoparticles show bandwidth increases with increasing particle diameter, when the diameters are > 20 nm. Figure taken from [10]. (b) The absorption coefficient of Ag when particle diameters are < 20 nm. The peak broadens as the particle diameter decreases, confirming a 1/R relationship in this region. Figure taken from [15].*

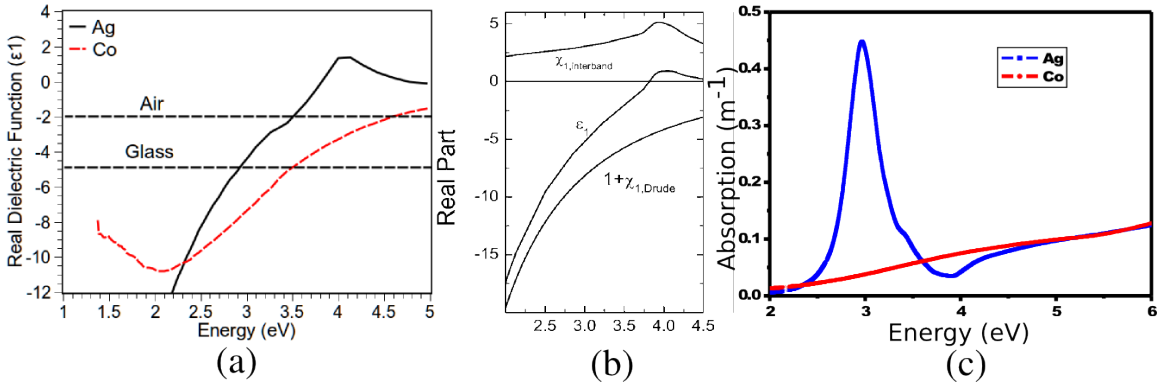


Figure 1.4: *(a) The real parts of the dielectric function (ε') for Ag (solid line) and Co (dashed line) as a function of energy. The intersection of the dielectric functions with the air line ($\varepsilon' = -2$) and SiO_2 line ($\varepsilon' = -4.9$) is also shown. At these intersections the metals will show plasmon resonances in the respective host medium. Figure taken from [16]. (b) The real part of the Ag dielectric showing the contribution from interband transitions and the Drude contribution. Figure taken from [17]. (c) Absorption coefficient for Ag and Co nanoparticles embedded in SiO_2 host matrix with a volume fraction of 5%. It can be seen that the LSPR for Co is completely suppressed because of its proximity to the Co interband transition of 3.8 eV. However the Ag LSPR is extremely sharp. Figure taken from [16].*

1.2.2.3 *LSPR of Ag*

The energy dependence of the real part of the dielectric function for Ag is shown in Fig. 1.4(a) as a solid curve and the contributions from interband and intraband transitions in Fig. 1.4(b). For Ag in a glass (SiO_2) host ($\varepsilon_h \sim 2.4$), the Mie condition for a plasmon is satisfied at an energy of ~2.9 eV (~428 nm), shown by the intersection of the curve for ε'_{Ag} with the $\varepsilon' = -4.8$ line in Fig. 1.4(a). This energy is below the strong interband (d-sp) transitions at ~4 eV, as shown in Fig. 1.4(b). As a result, the plasmon in Ag is extremely sharp because the primary dephasing pathway in Ag corresponds to radiative decay and the elastic scattering processes. In contrast, Au and Cu have weaker plasmons due to the proximity of broad interband transitions to the plasmon energy [11].

1.2.2.4 *LSPR of Co*

Co (and the other ferromagnetic metals) satisfies the Mie condition of $\varepsilon'_{Co}(\omega)$ = -2$\varepsilon_h(\omega)$ for the appearance of an LSPR in the ultraviolet range. Shown in Fig. 1.4(a) as a dashed curve, $\varepsilon'_{Co}(\omega)$ is found to intersect the air (-2) and glass (-4.8) dielectric lines at ~4.5 and 3.5 eV, respectively. However, they are generally not visible in the far field UV-Vis optical spectroscopy experiments. Theoretically calculated Co band structure shows a number of direct transitions between the $d-sp$ bands, centered at 3.8 eV with a width of ~3.4 eV [18], which severely dampens the plasmon excitations.
The distinctive plasmonic behavior of Ag and Co can be compared by evaluating the theoretical absorption coefficient of nanoparticles based on a Maxwell-Garnett approximation, in which $\alpha(\omega)$ is given by [19]

$$\alpha(\omega) = A\frac{\omega\varepsilon''_m(\omega)}{[\varepsilon'_m(\omega) - 2\varepsilon_h]^2 + [\varepsilon''_m(\omega)]^2} \tag{1.5}$$

where A is a constant representing the volume fraction of the metal in the host. In Fig. 1.4(c), the behavior for Ag and Co nanoparticles embedded in SiO_2 host matrix with 5% volume fractions was compared [19]. It is clear that the absorption coefficient for Co does not show a Localized SPR, while for Ag the resonance is sharp and narrow, as expected.

1.3 Principle of LSPR sensing

A widely established technique for sensing of molecular-level chemical and bio-chemical changes, such as in bio-molecular interactions, is to utilize the surface plasmon resonance (SPR) of ultrathin Au films [Fig. 1.5(a)]. In this technique, light is reflected from the interface between the dielectric substrate and the Au film. When the surface plasmon polariton (SPP) is excited at the Au-dielectric interface, the *intensity of the reflected light is at a minimum* for a specific reflection angle (or light frequency) due to the plasmonic absorption. Sensing or detection is achieved when the refractive index (n) or dielectric function (ε) of the environment in contact with the Au film changes. This leads to a shift in the SPR frequency and/or angle and measuring this change leads to sensing. In the case of bio-molecular detection, the selectivity to desired analytes come by choosing the immobilized interrogation species to have preferential binding to the analyte

[20, 21, 22, 3]. Presently there is a strong interest in moving towards LSPR sensing using nanoparticles as compared to SPR sensing, which uses smooth films. One of the primary limitations is that the excitation of surface plasmon polaritons requires that the incident light be total internally reflected at the metal substrate interface and hence configurations such as the Kretschmann geometry must be used [4]. On the other hand, nanoparticles can scatter efficiently in many directions, permitting more flexibility in sensing with light in reflection and/or transmission geometries. Additionally, the excitation of the LSPR on a nanoparticle requires irradiation by light of the LSPR frequency and it can be done at any angle. Therefore, utilizing nanoparticles could reduce the complexity of the sensor design vis-a-vis plasmon excitations.

1.3.1 Sensing with Nanoparticles

In contrast to the thin film, LSPR sensing of chemicals and environmental changes takes place by measuring changes in the wavelength of light transmitted or reflected from the nanoparticle-environment interface [Fig. 1.5(b)]. The wavelength change results from change in the dielectric or refractive index at the NP-environment interface, as evident from the Mie condition $\varepsilon'_m(\lambda) = -2\varepsilon'_h(\lambda)$. For the sensing to work, the incident light must contain a broadband of wavelengths around the known LSPR position. The measurement itself is quite straightforward since it can be performed in transmission or reflection geometry by utilizing a widely available broadband optical spectrometer coupled to a broadband light source. An example of LSPR sensing based on using Au nanoparticles is shown in Fig. 1.5(b).

In generic terms, the sensitivity of the technique can be defined as the measure of how much the output changes with respect to a small change in input. For LSPR, the input is the change in refractive index of the medium and the output is a change in wavelength. Quantitatively, the LSPR sensitivity is defined as $S = \frac{d\lambda_{LSPR}}{dn}$, where λ_{LSPR} measures the LSPR wavelength (*in nm*) as a function of varying refractive index n (*in refractive index units RIU*), thus giving S in nm/RIU. Examples of broadband optical absorbance measurements capturing these LSPR changes are shown in Fig. 1.6(a), where the scattered light of Ag nanoparticles is shifted towards the red wavelength as the dielectric function of the medium increases. The values for sensitivity are obtained by generating a trend of the LSPR peak positions to the refractive index of the different mediums used, as in Fig. 1.6(b). The slope of this scatter plot is the sensitivity S of the plasmonic material system used.

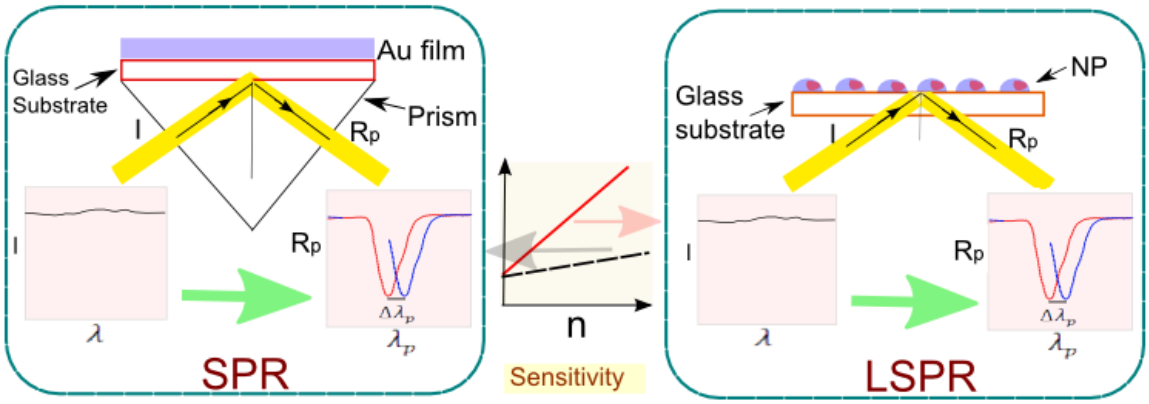
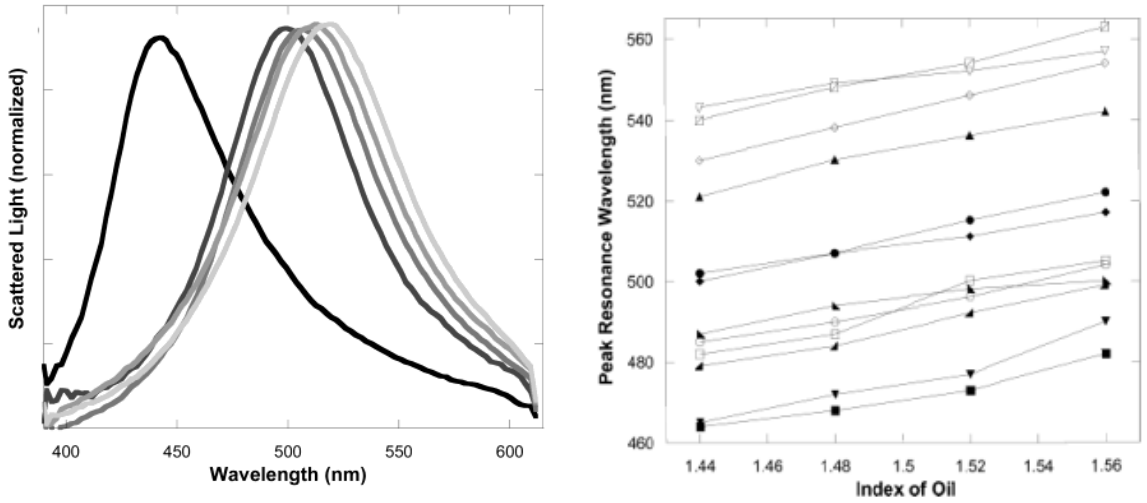


Figure 1.5: *SPR vs LSPR sensing. (a) In SPR sensing, shift in plasmonic wavelength of $\Delta\lambda_P$ at the total internal reflection angle of the prism - metal interface (Kretschmann geometry), corresponding to SPR excitation, is measured and correlated with change in refractive index n due to chemical interactions on the metal surface. (b) In LSPR sensing, the relative change in reflectivity R_p at the LSPR resonance. The increased sensitivity of NP to change in n is due to the ability to differentiate small changes in R_p with chemical changes [23]. This increased sensitivity for NP is shown in the center panel as the trend line with larger slope for the behavior of measured signal versus n.*



(a) (b)

Figure 1.6: *(a) Scattered light of Ag nanoparticles as refractive index of liquid is changed, from air (n=1.00) to various oils (starting from n=1.44). (b) Sensitivity plots derived from normalized spectra in (a). The peak positions are maxima of extinction spectra at specific wavelengths, on the y-axis. The indices of the oil are plotted on the x-axis. The slope from these plots constitutes the sensitivity of the measurements in units of nm/RIU. Figures taken from [24].*

1.4 Current challenges in LSPR sensing

The current-state-of-art in commercially available LSPR sensing is based on utilizing Au nanstructures. As can be gleaned by information provided in commercial websites, the S value for Au LSPR sensors is approximately 80 nm/RIU [25]. Currently, research into Au nanostructures has demonstrated sensitivity in the range of 90-703 nm/RIU shift, as shown in Table 1.1.

As mentioned earlier, visible wavelength localized surface plasmons primarily occur in nanoparticles of noble metals (Ag, Au and Cu) and alkali metals (Na, K). Visible wavelength plasmons are clearly essential towards simple and cost-effective LSPR sensing applications. However, the materials limitation is very important. In addition, as evident from the definition of the figure of merit, materials with sharp plasmons (i.e. narrow bandwidth) will be most useful. In this context, Au, Ag and Cu all have strong plasmonic properties in the visible optical spectrum because of their long electron relaxation times [10]. However, Ag has the highest optical scattering cross-section, more than 4 times of Au or Cu [10]. However, Cu is known to oxidize very rapidly and, as such, is not considered to be a practical plasmonic metal. Surprisingly, Ag also degrades rapidly in air, though at a rate significantly slower then Cu. In addition, the lower cost of Ag and the fact that it is over 70 times more abundant than Au, makes it the best choice for visible light plasmonic-related applications. Figure 1.7 shows the quantitative plasmon quality of various materials, expressed as *QLSP*, where this is defined as the maximum quality of the localized surface plasmon. As can be seen, Ag has a high quality plasmon number, along with Au and Cu, yet it is not nearly as expensive as Au and does not oxidize as quickly as Cu.

The use of Ag as a long-term plasmon metal in oxidizing environments is uncertain and the corrosion of the bulk Ag surface in ambient air conditions has been studied in some detail. One picture is that Ag can react with several different species in the ambient environment, with the resulting corrosion products being oxides, sulfides, or chlorides [26]. More recently, with the growing emphasis on plasmonic applications, Ag nanostructures exposed to oxidizing environment have shown evidence that corrosion substantially changes the optical plasmonic signal, such as a decrease in the plasmonic absorption intensity and a shift in the LSPR wavelength (λ_{LSPR}) [27]. Therefore, the current understanding of Ag degradation with respect to the optical plasmonic behavior is that the corrosion product related dielectric, such as Ag_2O, produces a shift in λ_{LSPR} and decay in the LSPR signal intensity. Moreover, as a function of increasing time under storage or operation conditions, the average size, shape, and distribution of Ag could also change, again producing uncertainty in the λ_{LSPR} [28, 29]. Therefore, one of the outstanding challenges in this field is to find more cost-effective and better plasmonic metals then Au.

Table 1.1: *Table above shows various sensitivity (nm/RIU) values for different Au nanostructures based on size and number of particles (single or array). Table taken from ref. [6].*

			λ_{peak}		$\Delta\lambda$		shift/RIU		
ref	partide	type	nm	eV	nm	eV	nm	eV	FOM
Chen 2008[43]	Au branches	ensemble	1141	1.09	879	0.983	703	0.415	0.8
Tam 2004[46]	Au/SiO_2 shell	ensemble	770	1.61	350	0.732	314	0.657	0.9
Sun 2002[47]	Au/AuS shell	ensemble	700	1.77	400	1.01	409	1.04	1.0
Wang 2006[48]	Au nanorice	ensemble	1600	0.775	600	0.291	801	0.388	1.3
Mayer 2008	Au nanorod	ensemble	720	1.72	125	0.301	170	0.327	1.3
Underwood 1994[49]	Au sphere	ensemble	530	2.34	60	0.265	090	0.397	1.5
Raschke 2004[50]	Au/AuS shell	single	660	1.88	77	0.220	117	0.333	1.5
Sherry 2005[21]	Ag cube	single	510	2.43	91	0.433	146	0.695	1.6
Malinsky 2001[51]	Ag NSL	ensemble	564	2.20	104	0.405	191	0.745	1.8
Nehl 2006[17]	Au star	single	675	1.84	125	0.340	238	0.649	1.9
Lee 2009[52]	Au pyramid	single	680	1.82	114	0.310	221	0.450	2.2
Mock 2003[53]	Ag sphere	single	520	2.38	73	0.335	160	0.734	2.2
Bukasov 2007[54]	Au crescent	ensemble	1795	0.69	209	0.080	596	0.190	2.4
Khalavka 2009[55]	Au rattle	single	570	2.18	52	0.198	199	0.568	3.8
Mock 2003[53]	Ag triangle	single	760	1.63	80	0.172	350	0.751	4.4
Burgin 2008[56]	Au bipyramid	ensemble	681	1.82	52	0.140	352	0.620	4.5
Sherry 2005[21]	Ag cube-sub	single	430	2.88	22	0.146	118	0.792	5.4
Nehl 2006[17]	Au star	single	770	1.61	124	0.260	665	1.41	5.4

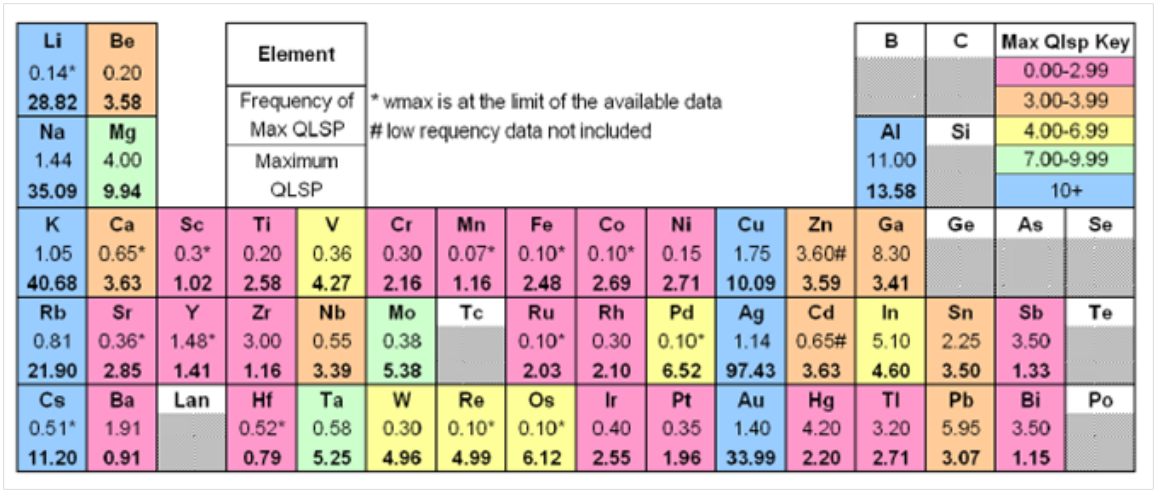


Figure 1.7: *The figure above shows the various materials and their plasmonic maximum QLSP which describes the maximum quality of the surface plasmon resonance. It is shown that Co has a low plasmon quality while Ag has a high quality plasmon, comparable to Au and Cu. Figure taken from ref. [11].*

1.5 Outline of Thesis

In this thesis we have extensively investigated the plasmonic behavior of AgCo nanoparticle arrays. The bimetallic AgCo system was chosen for various reasons. As mentioned in the previous section, there is urgent need for plasmonic materials which have comparable or better sensitivity than Au but with significantly reduced cost. In this regard, Ag and Co are both very inexpensive. However, as mentioned, Ag has the tendency to degrade due to oxidation. Over the past few years, mixing of Ag with various metals, primarily Au, has been investigated as a route towards a metal with higher chemical stability as well as good plasmonic properties. However, the AgAu system has not shown significantly enhanced stability. Electronic effects at the Ag-Au interface and/or the formation of the alloy has been suggested in the observed lack of stability of the AgAu system [30, 31, 32]. This is partly due to the high reduction potential of Au, which causes Ag to be oxidized, and/or due to the complete miscibility of the two metals, which drives alloy formation. Thus far, no clear resolution to achieving stable Ag nanostructures has been found. Recently, research by our collaborators has demonstrated that nanoparticles of the AgCo system can show a large tunability in the location of the LSPR wavelength as a function of the size and composition of the two metals [1]. Based on this early success, we have focused this thesis research on investigating the AgCo system, especially the wavelength and quality (bandwidth) of the plasmons as well as its sensitivity and figure of merit in LSPR sensing application and the stability of the material to environmental degradation. An outline of the various contents in this thesis is provided below.

1.5.1 Outline

- Chapter 2: *Experimental Procedures and Results*

  The synthesis techniques to make AgCo and Ag nanoparticle arrays are explained in the first part of this chapter. Electron beam (e-beam) deposition was used to form Ag or AgCo bi-layer films. Pulsed laser irradiation was carried out on the films to create dewetted nanoparticles of different particle size and composition [33]. To test the effects of oxidation on the nanoparticles, these samples were exposed to ambient air at room temperature for up to six months as well as annealed at various temperatures (50, 100, and 150^{o}C) for 100 minutes. After this sample processing was completed, characterization was performed on the samples using a UV/Vis spectroscopy to analyze usefulness towards LSPR sensing. Afterwards, atomic force microscopy was used to see what dimensional changes occurred in annealed samples. Finally, LSPR sensing measurements were also made on these samples

  Several results will be presented in the remainder of this chapter. Primarily the optical absorbance curves (both raw and normalized) are shown for the various samples and processing treatments. The plots show the location of the LSPR peak as well as changes to its wavelength and intensity.

- Chapter 3: Discussion

  This chapter discusses and analyzes the experimental results obtained from investigating AgCo and Ag nanoparticle arrays as LSPR sensing platforms. The bandwidth and LSPR peak were evaluated as a

function of particle size and Ag % composition. Using the size and composition parameters, the LSPR functionality of these metallic systems was evaluated by looking at the sensitivity. We found that AgCo is comparable to, if not, more sensitive than pure Ag. Low temperature (room temperature up to 150^{o}C) annealing experiments in ambient conditions were also performed to compare the stability of the AgCo to Ag systems, and we found that AgCo was significantly more stable than pure Ag. Overall, the AgCo system is comparable to pure Ag in plasmonic behavior and significantly better than Ag with respect to environmental stability. These results also implied that the AgCo could replace Au as the metal of choice in LSPR sensing applications.

- Chapter 4: *Conclusions*

  The summary and future work will be mentioned here, emphasizing the important results found from these experiments. Future steps can be taken to expand upon the scope of the AgCo bimetallic system, such as adding biomolecules to create targeted nano-bio-sensors. Additionally, the morphological changes between AgCo and Ag need to be further studied as it seems to be a consequence of the oxide formation on the surface of the particle. Another possibility could be to use different metals with similar properties to discover more efficient and beneficial plasmonic materials, for example using copper with cobalt as a bimetallic system. Furthermore, hybrid ferromagnetic and noble metal nanostructures can be created to implement more control over plasmon resonances using the magnetic field.

Chapter 2

Experimental Procedures and Results

In this chapter we detail the various experimental procedures performed throughout these studies. Additionally, we will explain the different measurements and results on Ag and AgCo nanoparticle arrays aimed at investigating the behavior of the localized plasmon resonance (LSPR) characteristics (wavelength and bandwidth) with composition and size, its stability with exposure to ambient air under various conditions of time and temperature, and the change in LSPR wavelength with immersion in liquids of various refractive index. Some of the results presented here have been published in reference [34]. In addition, some of the supporting measurements were provided by my collaborators and are indicated where appropriate.

2.1 Experimental Procedures

2.1.1 Sample Preparation

2.1.1.1 Thin Film Deposition and Irradiation

Quartz pieces were cleaned through sonification in acetone, isopropanol, and water. They were placed into a vacuum chamber to undergo electron beam (e-beam) deposition. This technique formed thin films (1–10 nm) of Co and Ag on commercially available optical quality SiO_2 wafers. Two metal films were deposited consecutively to form bi-layer films. Varying compositions of Ag and Co were created to show a positive correlation between the AgCo structure, particle size, and LSPR sensing capabilities. Depositions of 5 nm pure Ag, 5nm Ag with 1 nm Co, and 2 nm Ag with 5 nm Co were made. These films were subjected to pulsed laser irradiation, in which the particles gradually dewet from the substrate. To form arrays of nanoparticles (NP), the films were irradiated with a neodymium-doped yttrium aluminum garnet (Nd-YAG) laser. Each laser pulse of 266 nm wavelength, had energy density of 90 mJ/cm^2, a temporal width of 9 ns, and was separated by 20 ms in time. This resulted in the formation of an array of AgCo NPs of average diameter of 85 nm. The same techniques were used to create Ag nanoparticle arrays with an average diameter of 105 nm. To create different size nanoparticles with the same Ag % composition, the film thickness ratios were maintained. Table 2.2 shows the ratios used for the different compositions. This synthesis process is explained further in [33] and was performed by collaborators. Table 2.1 shows the various combinations of nanoparticles used throughout this investigation.

2.1.2 Processing

2.1.2.1 Annealing

The samples were annealed on hot plates (Model PC-420, Corning and Scholar 170, Corning) for various temperatures (50, 100, and 150ºC) for 100 minutes to study the degradation process. A thermocouple, connected to a multimeter (Omega HHM31), was placed next to the sample on each hot plate, to record the temperature. Since the hot plate was exposed to the environment, the humidity of the surrounding, during annealing, was recorded with a humidity sensor (S/N 61623538, Fischer Scientific), to be approximately a constant 44% throughout the entire procedure. The ambient temperature was recorded as 22ºC. In another investigation, samples were stored in ambient air conditions at room temperature for various times ranging up to ~6 months.

2.1.3 Characterization

2.1.3.1 Optical Spectroscopy

A UV-VIS-NIR light source (DH-2000, Micropak) was used to transmit and detect light through optical fibers (P-600-2-SR, Ocean Optics and R-600-7-SR-125F, Ocean Optics). Using the spectrometer (HR2000+, Ocean Optics) and the software (SpectraSuite, Ocean Optics) that came with the instrument, spectra in the transmission mode were taken. Since AgCo nanoparticles were deposited on quartz, this allowed for the use of the transmission mode during optical measuring. To measure the sensitivity of the LSPR plasmon with Ag-Co concentration, this experiment was repeated in various mediums, tabulated in Table 2.3. To make sure the liquids were pure, the refractive index of these were measured using a refractometer (PAL-RI, Atago). Fig. 2.1 shows the set-up for the optical characterization. The UV-Vis light source is connected to an optical fiber through which it transmits its light to the sample, that is lying on a platform, that is pictured inside the green rectangle. Once the light is transmitted, it continues through the optical fiber attached underneath the platform, which serves as a detector. This fiber is connected to the spectrometer which collects the data and sends it to the computer via a usb connection. Before starting the optical measurements, the transmission spectra must be referenced against a quartz substrate as shown in Fig. 2.2. A piece of quartz substrate was placed alongside the sample, inside the beaker, as shown in Fig. 2.3 (a). The beaker was placed underneath the optical fiber probe after liquid was placed into the beaker. By keeping the volume of the liquid the same throughout, this ensured the distance between the probe and the sample would not change extensively, thus making the measurements more accurate. Once the beaker was placed and the liquid settled down, the measurement was taken at the center of the sample. In between measurements for different liquids, the samples and beaker were washed with distilled water to make sure no residue from previous liquids was left behind on the sample or in the beaker. After the measurements were taken, the transmission spectra were converted into absorbance using the equation, $A = log(100/T)$. FitYK software was used to obtain the LSPR peak and the FWHM of the curves, by fitting Lorentzian curves to the absorbance spectra.

Table 2.1: *The table below shows the various combinations of nanoparticles made with this synthesis technique.*

Material	Particle Diameter [nm]	Composition
Ag	70,90,110	100%Ag
AgCo	70,90,110	83% Ag-17% Co
AgCo	70,90,110	72% Ag-28% Co

Table 2.2: *Film thickness ratios listed along with the particle diameters.*

Material	Composition	Film Thickness Ratio	Particle Diameter [nm]
Ag	100%	5	70,90,110
Ag/Co	83% Ag-17% Co	5/1	70,90,110
Ag/Co	72% Ag-28% Co	5/2	70,90,110

Table 2.3: *Mediums used for optical experiments.*

Mediums	*Refractive Index*
Air	1.00
Water	1.33
Isopropanol	1.37
Glycerol	1.47

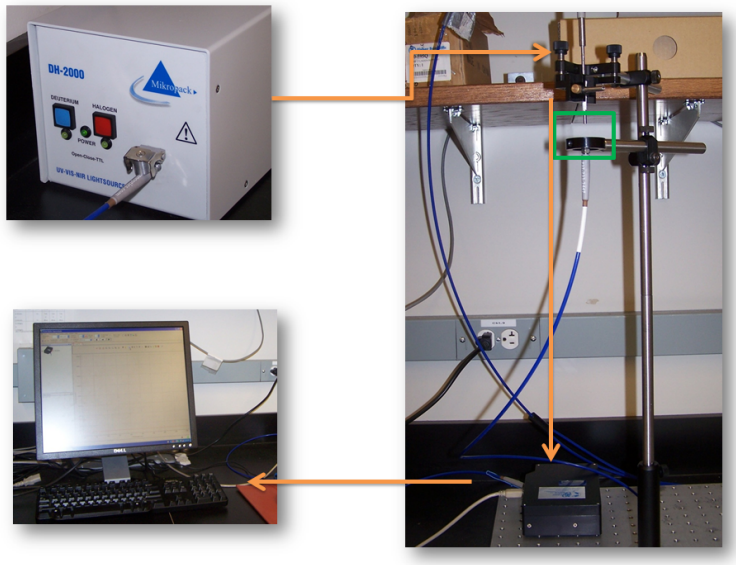


Figure 2.1: *Optical set-up for the sensitivity and oxidation experiments. The UV-Vis light source is connected to an optical fiber that transmits its light to the sample on the platform (area inside the green rectangle). The optical fiber serving as the detector is attached underneath the platform and this is connected to the spectrometer on the table. The spectrometer collects this transmission data and sends it to the computer via a usb cord. The data is then output into the Ocean Optics Spectra Suite software.*

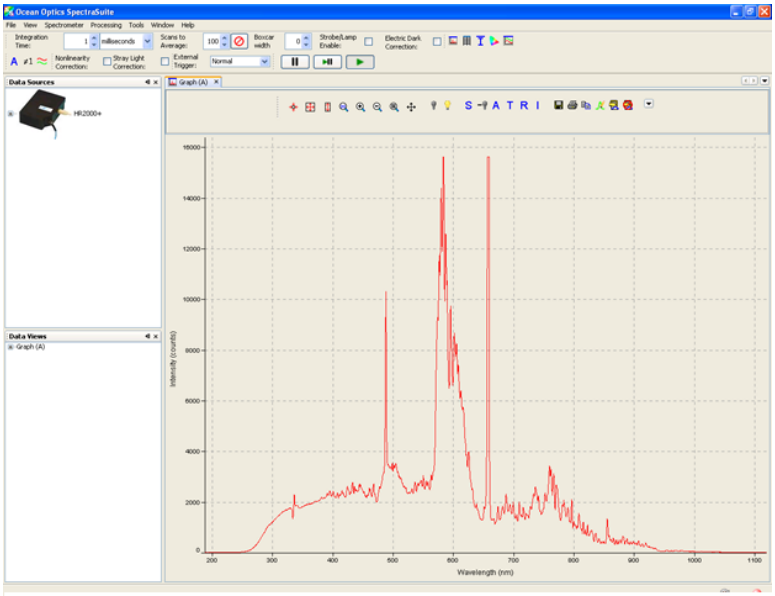
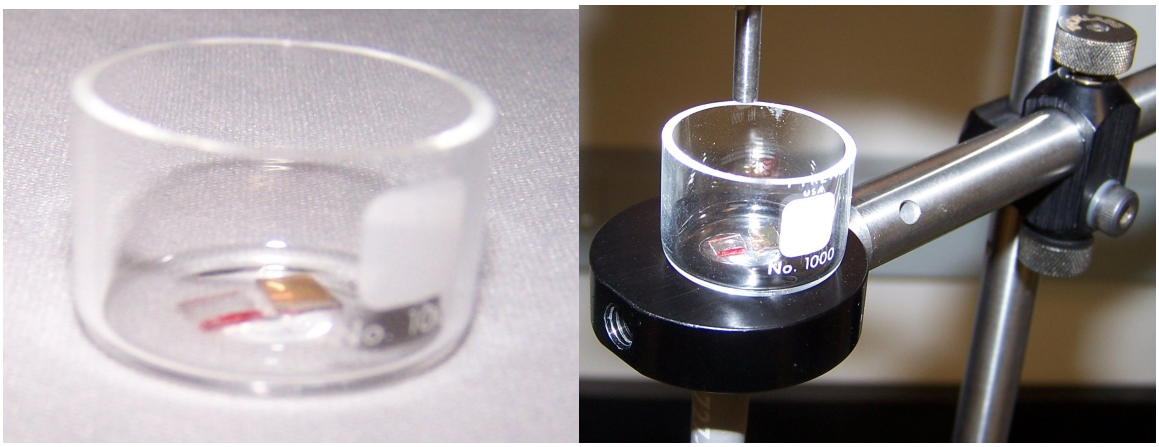


Figure 2.2: *Screenshot of Spectra Suite software showing reference spectrum on quartz substrate.*



(a) (b)

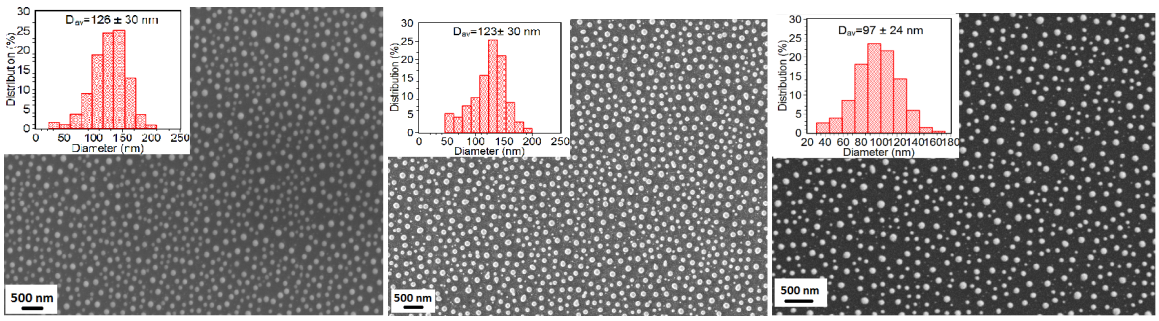
Figure 2.3: *(a) The container which was used to contain the different liquids during sensitivity experiments. A quartz substrate for the reference was placed inside as shown and the sample alongside it. (b) The optical fiber probe is lowered into the container as close as possible so the maximum transmission intensity can be obtained.*

2.2 Results

In Fig. 2.4, representative SEM images and size histograms are shown for the samples investigated here, namely the Ag and AgCo nanoparticle arrays prepared on SiO_2 substrates. This SEM measurement was performed by collaborators . The arrays typically had a narrow size distribution and a region of size of 100 $\times$ 100 μm^2 was investigated by transmission optical spectroscopy.

2.2.1 Absorption spectra as a function of composition and size

The raw absorbance spectra, shown, in Figure 2.5 [top panel], was calculated from the transmission spectra by using the equation $A = log(\frac{100}{T})$ where T is the transmission intensity value and A is the absorbance value. After converting this data, the spectra were normalized against the maximum peak intensity value in each curve, this being the y-value of the LSPR peak. This step is needed if one is to accurately evaluate the behavior of the bandwidth. On the bottom panel of Fig. 2.5, the normalized broadband absorbance spectra of AgCo nanoparticle arrays prepared on quartz substrates are shown for the three different compositions studied: 100% Ag [2.5(a)], 83% Ag [2.5(b)], and 72% Ag [2.5(c)]. For each composition, the spectra are also shown for arrays with different average particle diameters of ~70, 90 and 110 nm. Different diameters for the same composition were achieved by maintaining the same film thickness ratio. The primary information that can be obtained from these spectra are the location of the various spectral features, such as the localized surface plasmon resonance peak and the spectral width, otherwise known as the bandwidth. From these measurements, a few important features can be gleaned. First, as the composition of the Co increased, the location of the LSPR red shifted in wavelength. Secondly, the LSPR also red shifted with increasing particle diameter within any given composition. There is also a clear increase in bandwidth as Co is added to Ag. Table 2.4 shows the LSPR values obtained from the spectra, for each composition.



(a) (b) (c)

Figure 2.4: *SEM images taken for different Ag % compositions: (a) 100 % Ag (b) 83 % Ag-17% Co (c) 72% Ag-28% Co. Size histograms show a narrow distribution.*

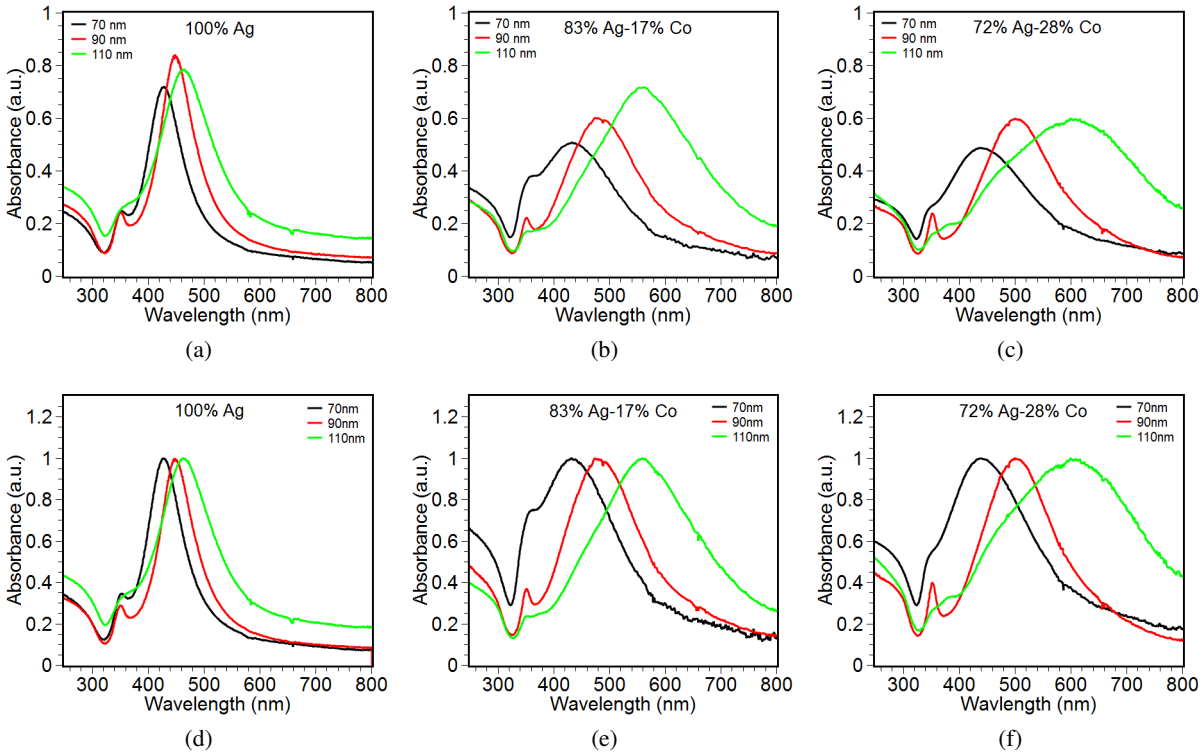


Figure 2.5: *Raw (unnormalized) absorption spectra for samples with varying Ag % composition (a) 100% Ag (b) 83.3% Ag-17% Co (c) 72% Ag-28% Co. In each figure, the spectra for arrays with different average particle diameter is also shown where the bandwidth difference between compositions is more noticeable.Normalized absorption spectra from samples with varying Ag % composition (d) 100% Ag (e) 83.3% Ag-17% Co Ag (f) 72% Ag-28% Co. In each figure, the spectra for arrays with different average particle diameter is also shown .*

2.2.2 Absorption spectra as a function of medium refractive index

Figure 2.6 [top panel] shows the raw absorption spectra of different compositions for 90 nm Ag and AgCo nanoparticles. In Fig. 2.6 (a) we see the spectra for Ag submerged in different liquids. There is a clear red shift as the refractive index of the liquid is increasing. This trend is also observed in (b) for 83% Ag-17% Co and (c) for 72% Ag-28% Co. These measurements were repeated for the 110 nm particle size with the same compositions, to determine the sensitivity AgCo as compared to Ag. The consistent behavior follows the prediction from the Mie Theory. Figure 2.6 [bottom panel] depict the normalized spectra for these samples. The shift is clearer when the spectra are normalized.

2.2.3 Absorption spectra as a function of time and temperature

In Fig. 2.7, the raw optical absorbance of 56$\pm$14 nm Ag particles and 85$\pm$18 nm 83% Ag-17% Co particles are shown as a function of time, measured in days, following storage in ambient air at room temperature. It is evident from the measurements for Ag, shown in Fig. 2.7 (a) that the LSPR peak at 468 nm decays in intensity with time. However, no significant change in the location of the LSPR wavelength is evident. The normalized absorbance of the measurements in Fig. 2.7 [bottom panel] are shown. This figure confirms that the width of the Ag LSPR [Fig. 2.7 (c)] peak width increases with increasing time, thus decreasing the plasmon peak intensity. In comparison, the AgCo [Fig. 2.7 (d)] shows a much smaller change in width.

The raw absorbance spectra of Ag (56nm) and AgCo (85nm) samples for different annealing temperatures are in Fig. 2.8 [top panel]. This data corresponds to a 100 minute annealing time condition. On the bottom panel of Figure 2.8, the absorption spectra for (c) Ag and (d) 83% Ag-17% Co were plotted. Here we can see a blue shift in the LSPR peaks for Ag as the annealing temperature is increased. Simultaneously there is a decay in the plasmon, noticeable by the the width increase and intensity decrease of the spectra. The shift is clearly not present in AgCo.

Table 2.4: *The extracted LSPR values from the absorbance spectra of different Ag compositions are listed below.*

Ag Composition	Particle Diameter [nm]	LSPR Position [nm]
	70	424
100% Ag	90	440
	110	450
	70	430
83% Ag-17% Co	90	488
	110	538
	70	443
72% Ag-28% Co	90	503
	110	582

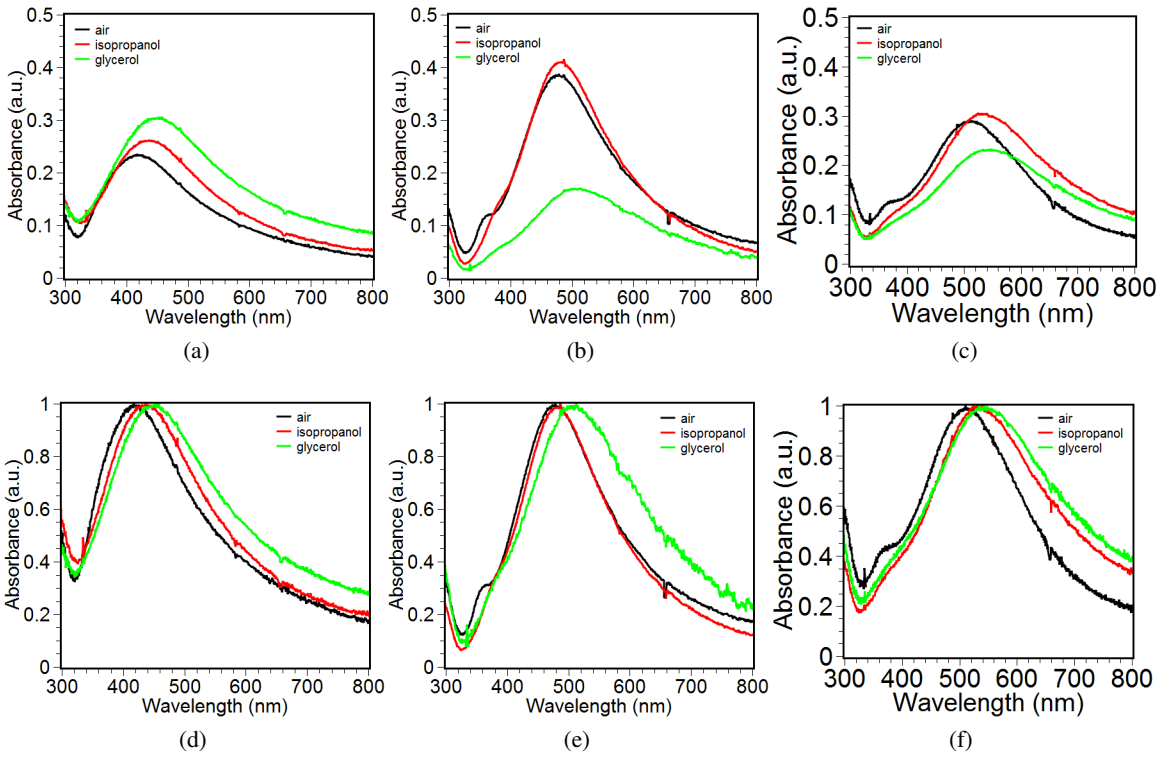


Figure 2.6: *Raw spectra of sensitivity measurements for 90 nm particles with different Ag % compositions: (a) 100% Ag (b) 83% Ag-17% Co (c) 72% Ag-28% Co. There is an obvious red shift trend seen as the refractive index of the liquid is increased, from air to glycerol. This behavior follows the Mie theory. Normalized sensitivity spectra of 90 nm particles for different compositions: (d) 100% Ag (e) 83% Ag-17% Co (f) 72% Ag-28% Co*

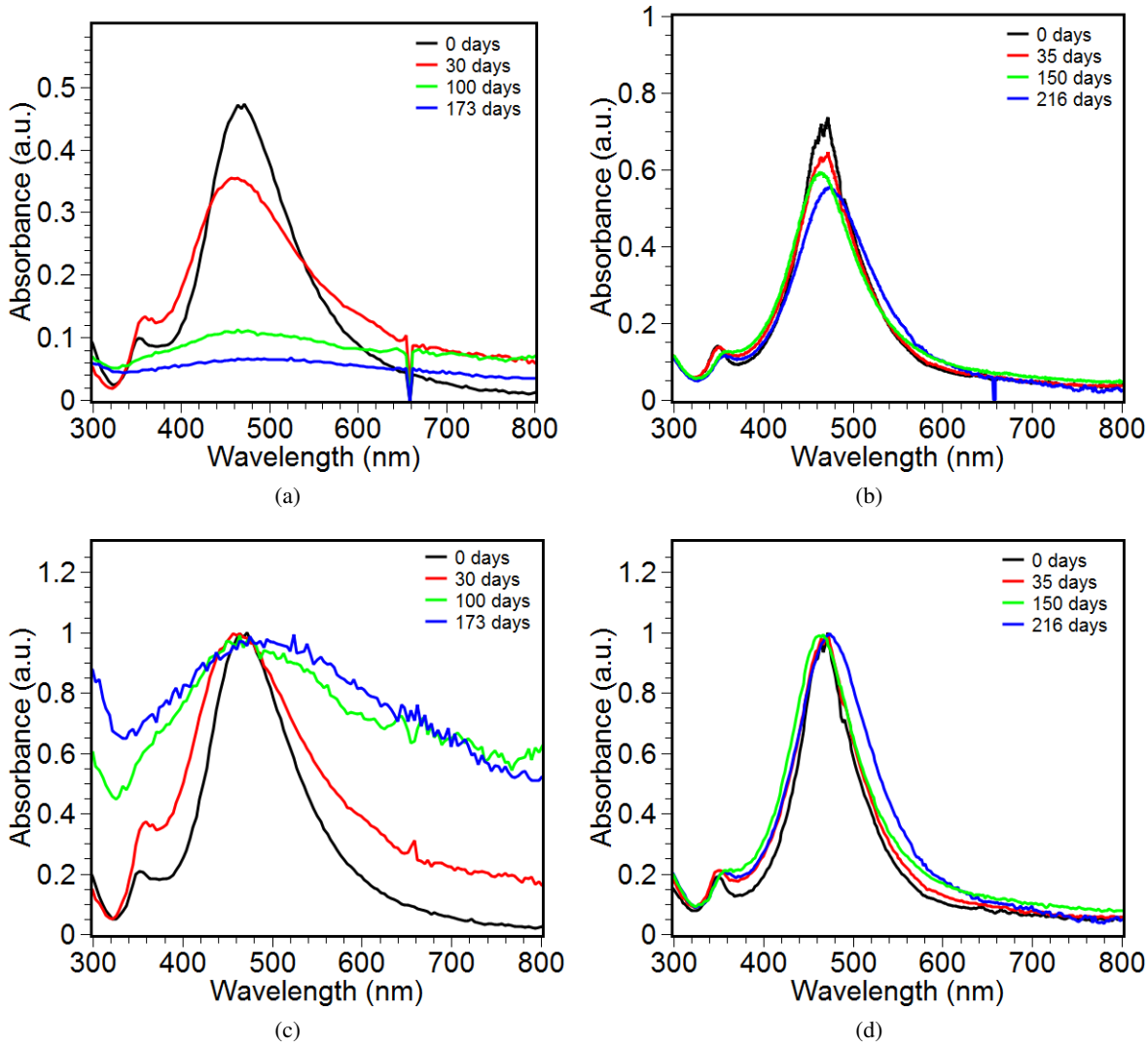


Figure 2.7: *Raw Absorbance spectra of (a) Ag with 56 nm average diameter and (b) AgCo (83% Ag-17% Co) with 85 nm average diameter, for various days following storage in ambient air at room temperature. Normalized spectra shown in (c) 100% Ag with 56 nm average diameter and (d) 83% Ag-17% Co with 85 nm average diameter.*

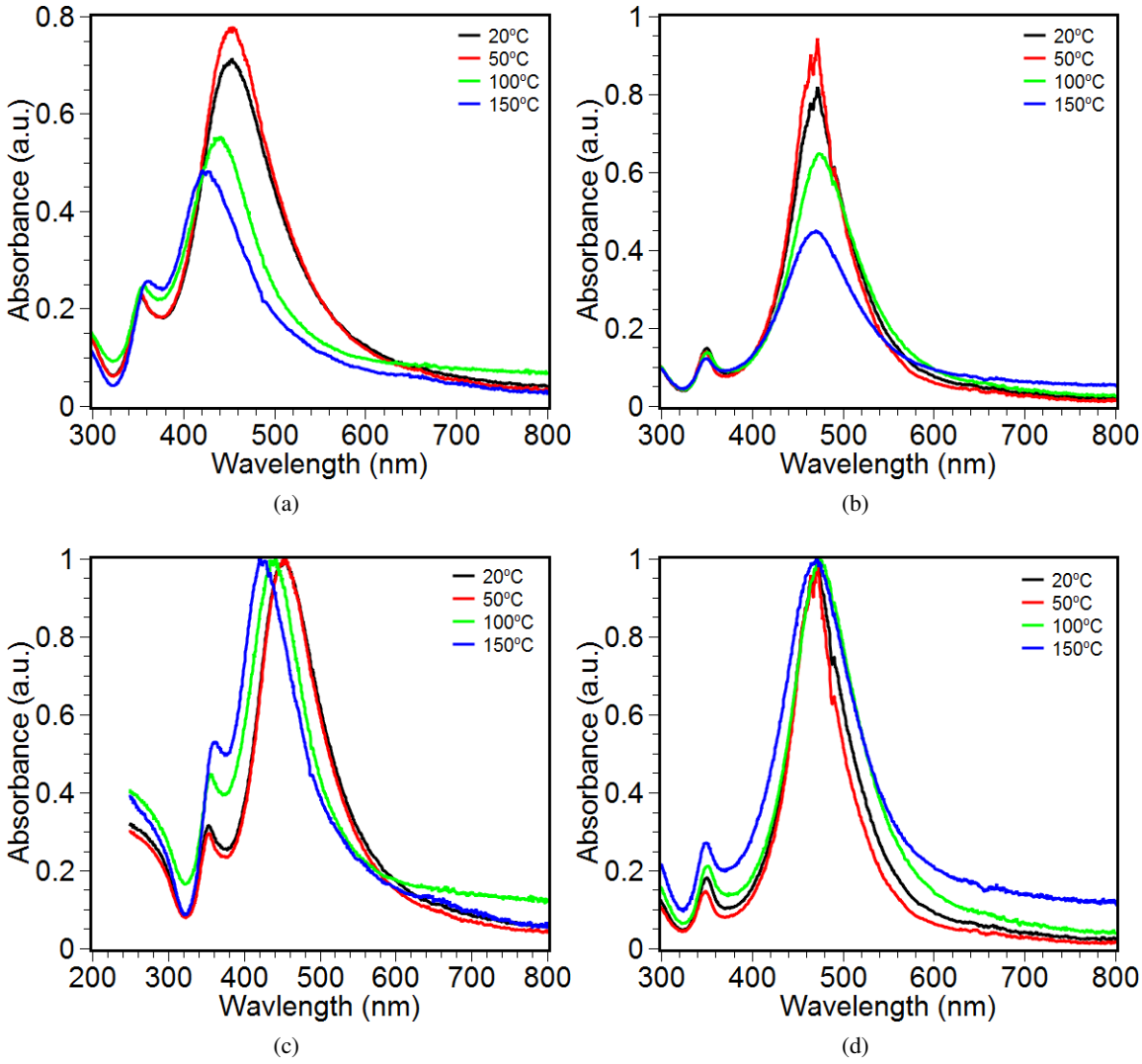


Figure 2.8: *(a) Raw absorbance spectra of a Ag sample annealed for 100 minutes at various temperatures. There is a general blue shift of the LSPR that can be seen in this data as well as the decay of the plasmon. (b) Similar spectra for AgCo annealed at 100 minutes for same temperatures. The LSPR here is not shifting throughout the annealing process. (c) Normalized absorbance spectra of Ag annealed at 100 minutes for different temperatures. The shift in the LSPR becomes clearer when the spectra are normalized. There is indeed a blue shift in the LSPR for Ag. (d) For the normalized AgCo (83% Ag-17% Co) spectra, the LSPR is not changing.*

Chapter 3

Discussion

This chapter of the Master's thesis analyzes and discusses the primary results shown in Chapter 2, which include, (i) tunability in AgCo LSPR wavelength with size and composition, (ii) dependence of bandwidth on size and composition, (iii) sensitivity to refractive index change on AgCo composition, (iii) dependence of LSPR on heat treatment in ambient air, and (iv) stability of the LSPR sensitivity measurements for AgCo nanoparticles heated in air.

I would also like to acknowledge here that several figures and discussions are taken from the reference [34] in which I am a co-author.

3.1 Tunability of Wavelength

In Fig. 3.1, the trends in the LSPR wavelength as a function of Ag concentration and nanoparticle (NP) size are shown. From the dependence on Ag concentration, shown in Fig. 3.1(a), the LSPR wavelength red-shifts with decreasing Ag content (experimental data in symbols). This behavior is consistently observed for the arrays with different average particle diameters, i.e. 70, 90, and 110 nm. In addition, the rate of shift appears to increase with increasing particle size. We have also plotted the experimental dependence on particle diameter, which is shown in Fig. 3.1(b), and the LSPR wavelength red-shifts with increasing size for any given Ag concentration. One of the practically relevant aspects of this result is the relatively large red-shift that can be achieved with increasing Co content and particle size. In other words, the wavelength of AgCo with 72% Ag can be tuned by ~200 nm by changing its size, in contrast to ~20 nm pure Ag over the same size. Therefore, we can claim a 10-fold tunability range in the LSPR wavelength by control of NP size and the amount of Co in the AgCo system.

To explain these results, we have incorporated the discussion taken from our collaborators and published in references [1, 34]. The LSPR shift with composition and size of the nanoparticles can be explained based on an effective medium optical model developed previously by our collaborators [35, 36]. Using this model, one can calculate the effective dielectric function of the bimetallic nanoparticle arrays on a glass substrate, such as shown in Fig. 3.2. Specifically, when the diameter D of a nanoparticle is less than the wavelength λ of light, such as in the present work, the optical response can be expressed as coming from a homogeneous medium with an effective dielectric function ε_{eff}. The calculation of the ε_{eff} is achieved in two steps. First,

by using the Maxwell-Garnett (MG) approach, the ε_{NP} for a nanoparticle made by grains of Ag and Co randomly arranged in the NP,as in Fig. 3.2, is calculated using the equation below:

$$\varepsilon_{NP} = \varepsilon_{Co} + \frac{3f\varepsilon_{Co}(\varepsilon_{Ag} - \varepsilon_{Co})}{\varepsilon_{Ag} + 2\varepsilon_{Co} - f(\varepsilon_{Ag} - \varepsilon_{Co})} \tag{3.1}$$

where ε_{Ag} and ε_{Co} are the complex dielectric permittivities of Ag and Co respectively, and f is the volume fraction of Ag in Co. In the next step of the model, the optical response of the NP array was modeled as a layer of thickness $h = D/2$ made from the hemispherical particles of average diameter D consisting of grains of Co and Ag, and embedded in a host medium of effective dielectric function ε_{host}, which is made from air and SiO_2 [1]. The effective dielectric function of the host medium is given by $\varepsilon_{host} = \varepsilon_{SiO2}\sigma + (1-\sigma)\varepsilon_{air}$, where the subscripts refer to the dielectric of the substrate and surrounding materials, and σ is the fraction of the nanoparticle area in contact with the substrate. For the case of hemispherical particles, σ is 0.33. In the final step, the MG mixing model of Eq.3.1 was applied self-consistently to obtain the final dielectric function with ε_{NP} and ε_{host}, with the volume fraction of particles given by $f = \frac{2\pi}{3}(\frac{D}{2\Lambda})^2$ where Λ is the spacing in between the nanoparticles and D is the diameter of the nanoparticle. From these calculations, the theoretical LSPR wavelength was generated as a function of composition and size, and this is shown by the trend lines on Fig. 3.1(a) and (b). Excellent agreement is seen with the experimental data, including the predictions of different red-shift magnitudes for the different sized particles. This result confirmed that the observation of Fig. 3.1(a) and (b) is a direct result of the size, shape, composition, and spacing of the nanoparticles, which are the only experimental parameters in the model.

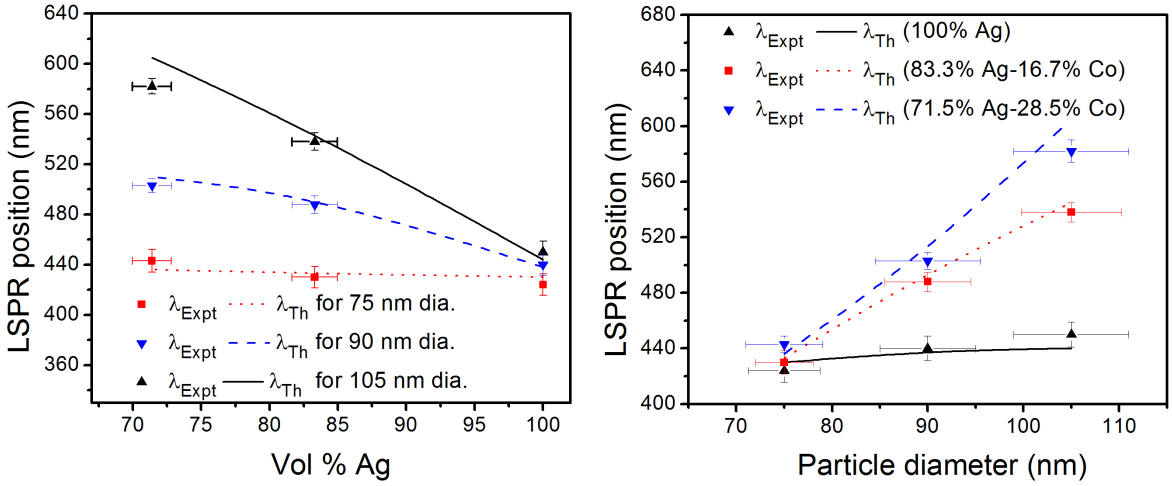


Figure 3.1: *(a) Experimentally measured LSPR shift (symbols) with varying Ag % for arrays with different average particle diameters. The position of the LSPR was obtained from the absorbance curves in Ch 2. (b) Experimentally measured LSPR shift (symbols) with varying particle size for various Ag %. The trend lines in both figures are results of effective medium modeling. The figures were taken from ref.* [34].

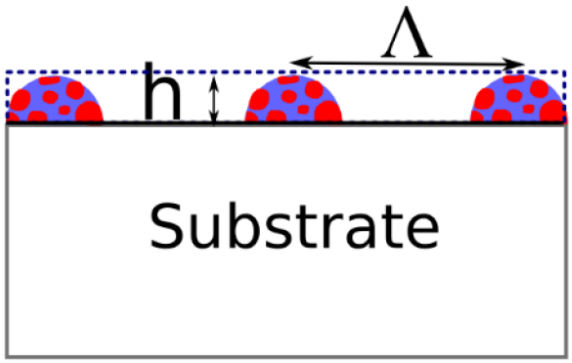


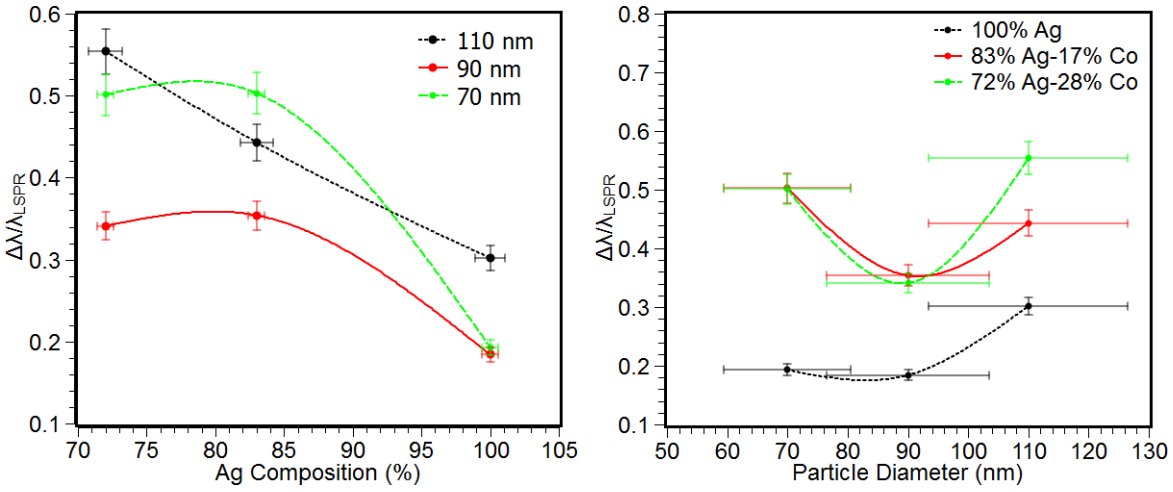
Figure 3.2: *The schematic model to estimate the effective dielectric function of the AgCo nanoparticle array layer formed by hemispherical particles of radius h on top of a SiO_2 substrate. The Ag and Co grains were assumed to be randomly distributed in the nanoparticle. The figure was taken from ref.* [1].

3.1.1 Bandwidth Dependence on Size and Composition

In Fig. 3.3, the trends in the bandwidth (FWHM) normalized to the LSPR wavelength is shown as a function of Ag concentration and nanoparticle size. From the dependence on Ag concentration, shown in Fig. 3.3(a), the normalized FWHM generally decreases with increasing Ag content. This behavior is consistently observed for the arrays with different average particle sizes, i.e. 70, 90, and 110 nm. We have also plotted the experimental dependence on particle size, which is shown in Fig. 3.3(b), and the normalized FWHM appears to show a 'u' shaped behavior, i.e. a minima with varying size in the range of 70 to 110 nm for all Ag % compositions studied. While the addition of Co generally increases the bandwidth, there appears to be no substantial difference in the normalized FWHM of the AgCo arrays made from ~72% and ~83% Ag. Table 3.1 lists the bandwidth values as a function of composition for different particle diameters.

The dependence on size observed in Fig. 3.3(b) can be explained in a qualitative manner based on the well known behavior of the elemental nanoparticles such as Au and Ag. As mentioned in the introductory chapter, the bandwidth of the LSPR is related to the decay mechanism of the plasmon excitation. As shown by Link and El-Sayed [10], the bandwidth varies as a function of size due to contributional changes in the various decay mechanisms. For example, when particles are < 10 nm in radius, the dominant decay mechanism is due to scattering at the NP surface and the electron relaxation time varies with size as $\frac{1}{\tau_{eff}} = \frac{1}{\tau_{bulk}} + \frac{v_f}{2d}$, where τ_{bulk} is the bulk relaxation time of the electron, v_F is the speed of the electrons close to the Fermi surface, and d is the nanoparticle diameter. As a consequence, the bandwidth increases with decreasing size in this regime. On the other hand, as shown in ref. [37], for large particle sizes, > ~100 nm, radiative decay becomes a dominant loss mechanism and increases with increasing size. The consequence of these opposing trends is a 'u' shaped behavior, as measured experimentally for Au nanoparticles by Link and El-Sayed [10]. We suggest that the trends shown in Fig. 3.3(a) is possibly of similar origin, despite the fact that the NP size appears to be too large for the size-dependent correction to relaxation time to be effective. It should be emphasized that transmission electron microscopy (TEM) investigations of the structure of the NPs performed by our collaborators [34] show that the individual Ag and Co regions are composed of grains whose size is significantly smaller then the overall NP size. Therefore, the observed 'u' trend could be attributed to this behavior.

The general increase in bandwidth with increasing Co concentration observed in Fig.3.3 (a) could be explained by an effective relaxation time based on the concept of the Mathiessen's rule, which states that the total relaxation rate is the arithmetic sum of the relaxation rates of the various components in the system. In this case, the effective medium relaxation rate of the system composed of Co and Ag should be given by $\frac{1}{\tau_{eff}} = \frac{1}{\tau_{Ag}} + \frac{1}{\tau_{Co}}$. The bulk relaxation times of Ag and Co are 37.9 and 6.52 fs respectively [38]. As a result, the effective relaxation rate of the AgCo system is shorter than that of pure Ag and hence the bandwidth increases upon addition of Co to Ag.



(a) (b)

Figure 3.3: *Experimentally extracted data for LSPR bandwidth normalized by the LSPR position as a function of Ag % (a) and particle size (b). On the y-axis is Bandwidth/LSPR peak ($\triangle\lambda/\lambda_{LSPR}$). The various lines are guides to the eye.*

Table 3.1: *Bandwidth values of the absorbance spectra as a function of composition for different particle sizes.*

(a)

Ag Composition	Bandwidth [nm] for 70 nm particles
100%	83
83%	218
72%	221

(b)

Ag Composition	Bandwidth [nm] for 90 nm particles
100%	83
83%	171
72%	172

(c)

Ag Composition	Bandwidth [nm] for 110 nm particles
100%	135
83%	248
72%	335

3.2 Sensitivity Dependence on Composition

As discussed in the introductory chapter of this thesis, a change in the dielectric medium surrounding the plasmonic metal changes the wavelength of the LSPR and this can be understood through the Mie condition relating the real part of the dielectric function of the metal and the surrounding host, $\varepsilon'_m(\lambda) = -2\varepsilon'_h(\lambda)$. This phenomenon is the basis of the SPR sensing technique and one of the goals in the design of new SPR sensing materials is to have the largest possible change in wavelength for the smallest change in host dielectric. In practical terms, the measure of this change is evaluated by a quantity known as the sensitivity S, which is defined as the slope of the trend in LSPR wavelength (in nm) to refractive index n of the surrounding medium (in refractive index units, RIU), i.e. $S = \frac{d\lambda_{LSPR}}{dn}$.

In Fig.3.4 the change in λ_{LSPR} with n for various AgCo nanoparticle sizes and compositions is shown. The three different compositions, 100, 83, and 72% Ag as well as two different sizes for each composition, 90 and 110 nm, are shown. The general behavior in each case is a linear red shift with increasing n. The slopes of the individual curves, which corresponds to the value S, are also indicated in the figure. AgCo particle arrays show sensitivities of 51 and 71 nm/RIU respectively for 90 nm sized nanoparticles with composition of 83% Ag and 72% Ag, whereas 110 nm sized AgCo particle arrays show sensitivities of 105 and 56 nm/RIU for the 83% Ag and 72% Ag compositions. Also shown by the square symbols are the results for pure Ag nanoparticle arrays with particle diameters of 90 (solid square) and 110 nm (open square), which show sensitivities of 62 and 60 nm/RIU respectively. These measurements indicated that the sensitivity of the AgCo bimetallic arrays, which ranged between 51 and 105 nm/RIU, was similar to or larger than pure Ag particles of similar shape and size, despite the bimetallic particles having a larger LSPR bandwidth as compared to pure Ag. Below, in Table 3.2, the values corresponding to each particle diameter and composition can be seen.

The comparable or better sensitivity of the AgCo in comparison to Ag could be of significant practical relevance in applications to SPR sensing for several reasons. First, as evident from Fig. 3.4, the amount of Ag can be reduced by almost 30% while still achieving similar or better sensitivity than the pure Ag case. This is beneficial since it suggests a means to reduce the overall cost of the sensing material. Secondly, the laser dewetting synthesis route developed by our collaborators [34, 39] allows one to tailor the AgCo composition, size and spacing independently, which could lead to further optimization of the S values. In Fig. 3.5(a), a schematic illustration of the role of size on LSPR sensing can be presented in a simple manner. Consider a nanoparticle array with hemispherical particles of diameter D and spacing Λ, as shown in Fig. 3.5(a). If one assumes that the particle can detect a change in refractive index within a distance given by the LSPR decay length δ, then each particle has an effective LSPR size of $\frac{D}{2} + \delta$, denoted as D_{eff}, shown in Fig. 3.5(a). Therefore, the effective area of the substrate that is plasmonically active can be simply expressed as the ratio of the effective LSPR area to the area determined by the spacing of the particles, $\sim \frac{(D/2+\delta)^2}{\Lambda^2}$. In Fig. 3.5(b), we have plotted the measured values of S to the effective area ratio defined above using experimentally determined values of D and Λ and a decay length of $0.2 * (ParticleDiameter)$, which is the universal decay length scaling relationship for typical plasmonic nanoparticles [9, 10]. From Fig. 3.5(b) we can draw two conclusions. The first is that, in general, the addition of Co has not reduced the sensitivity over that of pure Ag. This can be seen from the fact that most of the values appear to fall within a range of

~50 to ~70 nm/RIU. A second is that some conditions of the AgCo system appear to give a much higher S value, as evidenced for the 83% case with 110 nm diameter particles, which has an S of 105 nm/RIU. The underlying reasons for these results are not clear. However, it is evident that a near-field understanding of the behavior of the plasmons and their decay with distance in AgCo could shed light on this behavior, as is being performed by my collaborators using EELS (Electron Energy Loss Spectroscopy) measurements in the TEM [40].

3.3 Stability and Sensitivity Dependence on annealing conditions

The results in Section 3.2, confirm that AgCo is a potential material candidate for applications in SPR or LSPR sensing and possibly other areas as well. In this section, we analyze and discuss the LSPR stability as well as plasmonic sensitivity S of the AgCo nanoparticle arrays following exposure to ambient air for various times and temperatures. This study is especially important since the biggest disadvantage that Ag has over the other useful plasmonic metal, Au, is its tendency to degrade rapidly in oxidizing environments [12, 26]. Several recent studies have shown that Ag nanostructures exposed to oxidizing environments undergo rapid decay of the optical plasmonic signal, including a decrease in the plasmonic absorption intensity and a shift in the LSPR wavelength (λ_{LSPR}) [27, 28, 41, 29]. The current understanding of Ag degradation with respect to the optical plasmonic behavior, is that the dielectric of the corrosion product, such as Ag_2O, produces a shift in λ_{LSPR} and decay in the LSPR signal intensity.

3.3.1 LSPR following room temperature storage

The simplest way to observe oxidative effects on the Ag and AgCo samples was to expose the samples to air for long periods of time and measure the plasmon peak behavior at various time intervals. In Fig. 2.7 in Ch. 2, we observed there is indeed a decay of the plasmon for Ag over time. Yet, under similar conditions, the AgCo (83 % Ag) did not show as large a degradation. In Fig. 3.6(a), the LSPR position of Ag (open symbols) and AgCo (closed symbols) is shown as a function of the number of days stored in air. The pure Ag array shows a change in wavelength that is not systematic as it undergoes a blue shift at early times and then a subsequent red shift. On the other hand, the AgCo is relatively unchanged. In Fig. 3.6(b), we have plotted the experimental, normalized inverse bandwidth, i.e. $\frac{\Delta\lambda_{LSPR}(t_o)}{\Delta\lambda_{LSPR}(t)}$ of the LSPR peaks as a function of time, where $\Delta\lambda_{LSPR}(t_o)$ corresponds to the bandwidth of a freshly prepared sample. It is clearly evident that the Ag particles (open symbols, dashed curve) degrade much more rapidly than the AgCo particles (closed symbols, solid line). In fact, the normalized inverse bandwidth of the pure Ag falls by 25% within 500 hours of exposure to ambient air while the AgCo requires more than 4500 hours for a similar amount of degradation, suggesting a nearly ten fold increase in the lifetime of the AgCo. Our collaborators have performed detailed transmission electron microscopy studies to analyze this result and concluded clearly that while the pure Ag oxidizes, the Ag in the AgCo does not. In fact, the only degradation to the AgCo system is the oxidation of Co with the formation of a +2 valence state of the Co [42]. It is known that for room temperature, the Co hydroxide formation rate with time follows an inverse logarithmic behavior [43]. In fact, our observation of the AgCo decay also follows a similar behavior, as shown by the solid

line in Fig.3.5 (b), described by a line equation, $y = 1.52 - 0.09ln(x + 274.5)$. The x value is the time in hours, and the output y value is the $\frac{1}{FWHM}$ value found. Ag is described by the exponential decay equation, $\frac{1}{FWHM} = 0.182 + 0.816exp^{\frac{-x}{1281}}$. The x in this equation denotes the time in hours and FWHM is determined from the experimental data. Therefore, in conjunction with the TEM results, the experimentally observed oxidation resistance of the Ag in contact with the AgCo was attributed to cathodic protection due to galvanic coupling. This phenomenon is likely analogous to that achieved by utilizing sacrificial anodes to stabilize bulk structures, such as bridges, underground pipelines, and hot water tanks [44]. Based on the standard electromotive force (emf) series [45], one can note that Co is significantly more anodic (E^o= 0.28 V for the reaction $Co \rightarrow Co^{2+} + 2e^-$) than Ag ($E^o$= -0.80 V for the reaction $Ag \rightarrow Ag^+ + e^-$). From this, one can reason that the spontaneous suppression of Ag oxidation, at the expense of Co, can occur if the overall potential of the reaction $2Ag^+ + Co = Co^{2+} + 2Ag$ is positive, which in this case is 1.88 V, and consistent with the experimental finding of stability of the pure Ag side of the NP, as compared to the pure Co side.

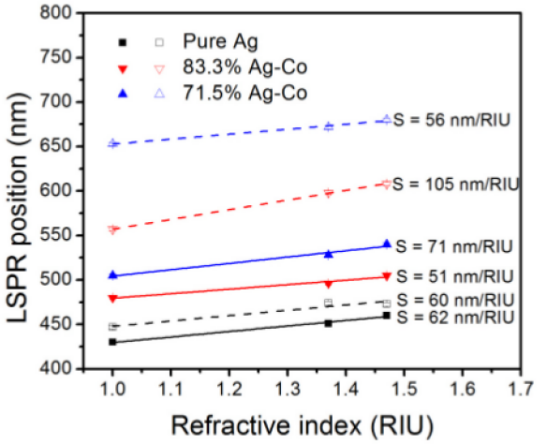
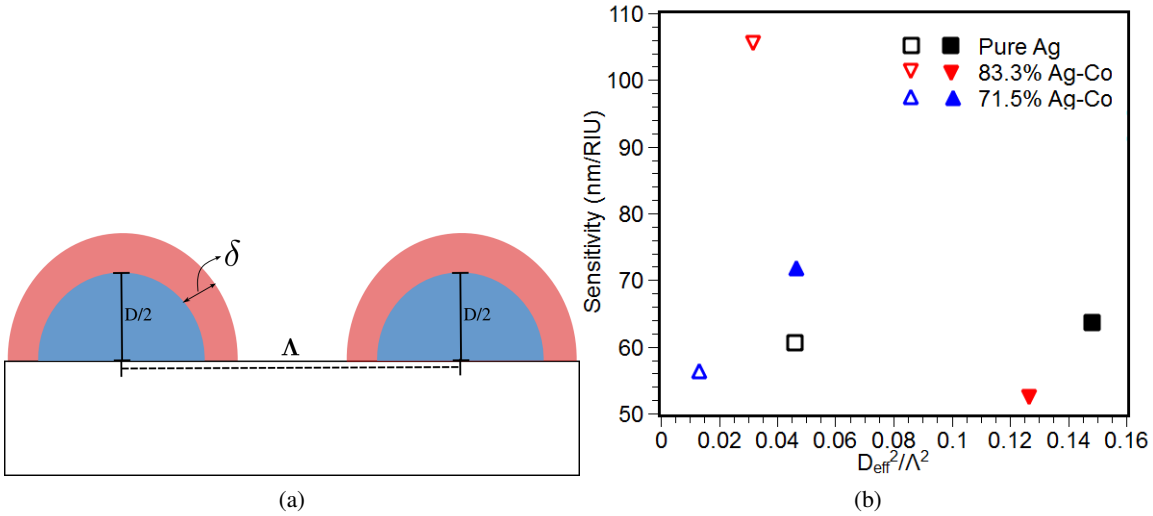


Figure 3.4: *LSPR wavelength change versus refractive index for the various Ag and AgCo systems for two different particle sizes. The filled symbols (solid lines) correspond to 90 nm particles and the open symbols (dashed lines) correspond with 110 nm particles. Figure taken from [34].*

Table 3.2: *Sensitivity values calculated from the slopes of the curves.*

Ag Composition	Sensitivity [nm/RIU] for 90 nm particles	Sensitivity [nm/RIU] for 110 nm particles
100%	62	60
83%	51	105
72%	71	56

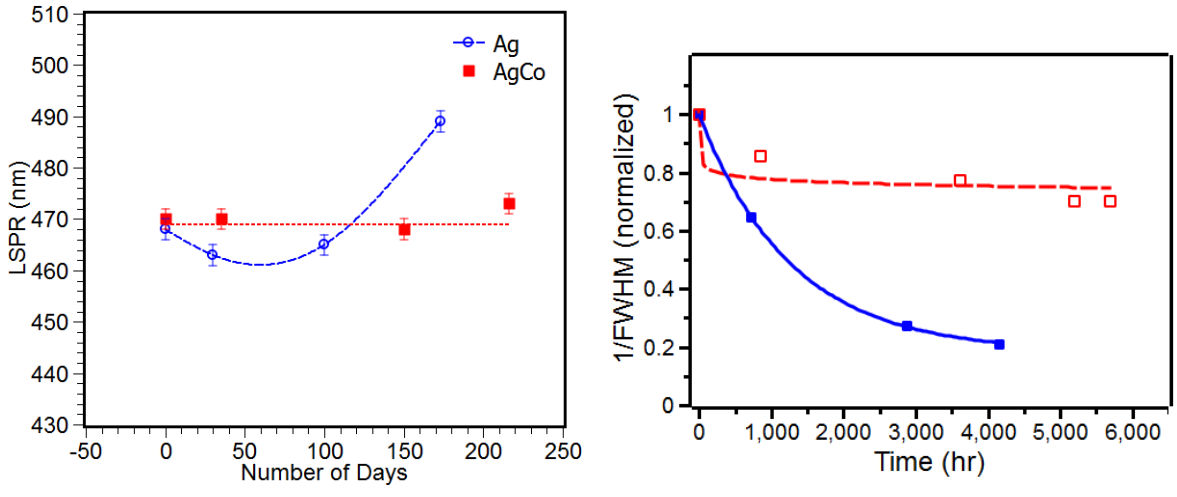


(a) (b)

Figure 3.5: *(a) Schematic illustration of the role of size on LSPR sensing. Hemispherical nanoparticles of diameter D are arranged on a surface with spacing* Λ*. The localized plasmon decay length around each particle is* δ *and determines the region within which refractive index changes can be measured. (b) Plot of the experimentally measured sensitivity S vs.* D_{eff}^2/Λ^2 *for ther various Ag and AgCo arrays investigated.*

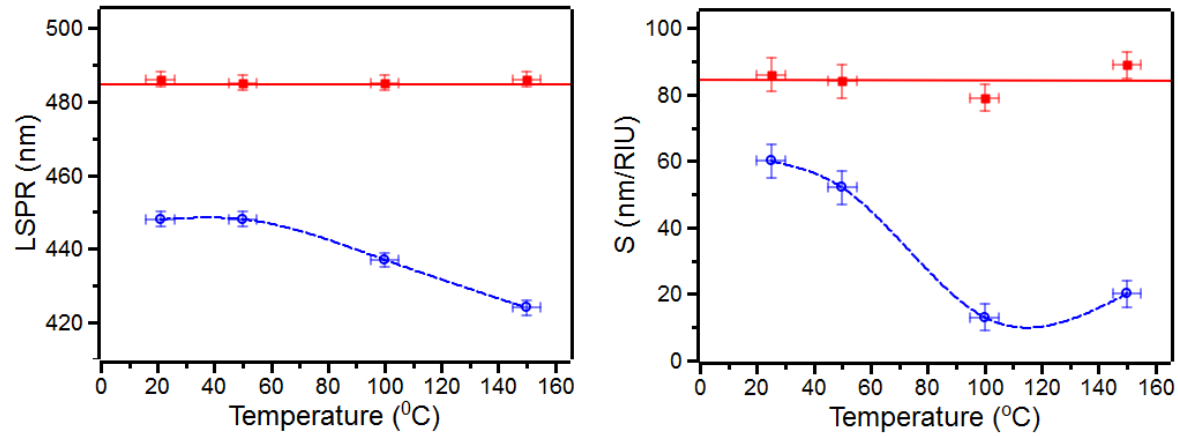
3.3.2 LSPR and sensitivity following high temperature oxidation

The LSPR wavelength changes for NP array (83% Ag-17% Co) samples following heating in ambient air for 100 minutes at various temperatures up to 150°C are shown in Fig. 3.7(a) for Ag (open symbols) and AgCo (closed symbols). From this figure it is apparent that the AgCo wavelength does not change within the heating temperatures investigated (the horizontal line shown is within uncertainty of a linear best fit trend). For the pure Ag case, the LSPR absorbance peak at ~450 nm [1] has blue shifted significantly following the heating. The LSPR sensitivity values for the NP array samples following heating in ambient air for 100 minutes are various temperatures up to 150° C are shown in Fig. 3.7(b) for Ag (closed symbols) and AgCo (open symbols). Once again, the AgCo shows a stable sensitivity value of ~85 nm/RIU over the heating temperatures investigated (the solid horizontal line shown is a guide to the eye). In contrast, Ag shows a substantial drop in S.



(a) (b)

Figure 3.6: *(a) LSPR wavelength versus number of days at room temperature for Ag (open symbols) and AgCo (closed symbols) (b) Normalized inverse bandwidth of the LSPR peak as a function if time at room temperature for Ag (closed symbols, solid line) and AgCo (open symbols, dashed line). Symbols are experimental data while the lines are fits to the behavior. Fig. (b) was taken from ref. [42].*

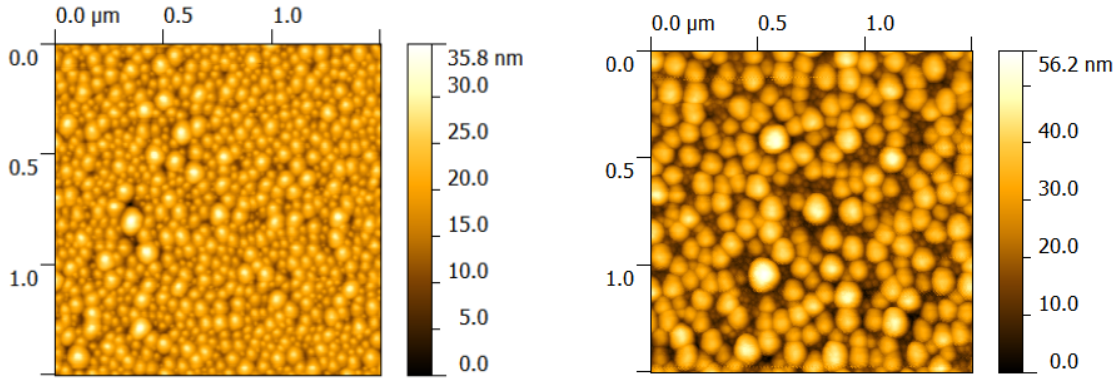


(a) (b)

Figure 3.7: (a) λ_{LSPR} following heating of the arrays in air at various temperatures for 100 minutes. AgCo data is shown by the closed square symbols while Ag corresponds to the open round symbols. (b) *Sensitivity of LSPR detection for arrays of pure Ag (open round symbols, dashed blue line is guide for the eye) and AgCo (closed square symbols, solid red line is horizontal guide line for the eye) for samples subjected to heating at various temperatures for 100 minutes.*

First we analyze the potential reason(s) for the blue shift in the Ag LSPR wavelength observed following heating in air [Fig. 3.7(a)]. In our previous results on the oxidation study in air at room temperature [Fig. 3.6(a)], an erratic behavior was observed, where first Ag underwent a blue shift and then for longer times, a red shift. From previous investigations on the behavior of Ag, it is known that oxidation of Ag leads to a red shift in the LSPR peak [27]. However, these previous studies were made for colloidal Ag nanoparticles dispersed in a solution. We suggest that in our case, there is also a large possibility that a Ag particle can ripen over time at room temperature or under heating leading to a change in the size and spacing of the particles. To corroborate this, our collaborators performed atomic force microscopy and SEM measurements comparing freshly prepared Ag and AgCo NP arrays to those following heating in air for 100 min at 100^{o}C. In Fig. 3.8, the AFM images of the as prepared Ag (a) and heated Ag arrays (b) are shown. It is evident that the average size of the Ag NPs has changed following heating. Analysis of the as prepared Ag array gave an average peak-to-valley height of 24$\pm$4 nm and diameter of 54$\pm$8 nm, and this changed to 36$\pm$5 nm and 46$\pm$7 nm following the heating. From this, it is possible to attribute the blue shift in the LSPR wavelength to an increase in aspect ratio or decrease in diameter of the particle [10], which is known to result in a blue shift. In contrast, SEM measurements of the AgCo did not show any measurable changes in the morphology following the annealing. This was another useful result and served to emphasize the stability of the AgCo system. The actual mechanisms underlying the lack of changes in AgCo and the shape changes in Ag need to be investigated in more detail as it likely involves a combination of the oxide formation, which will lead to an increased volume, as well as a relaxation of the metallic Ag shape from its quenched shape following the nanosecond pulsed laser dewetting synthesis. This idea could be pursued in detail by future researchers.

In Fig. 3.7(b), the sensitivity S for AgCo (closed symbols) is virtually unchanged while that of the pure Ag (open symbols) decreased significantly with increased heating. It should be emphasized that the S value of AgCo was measured with respect to the same starting λ_{LSPR}. On the other hand, for pure Ag, λ_{LSPR} varied for the different samples and from an application perspective, this would significantly increase the uncertainty of S values over that presented in Fig. 3.7(b). Based on the results presented here, it is clear that AgCo NP shows better structural and chemical stability against environmental oxidation, and thus significantly better stability in optical, plasmonic, and sensitivity behaviors.



(a) (b)

Figure 3.8: *(a) Atomic force microscopy (AFM) image of a freshly prepared Ag nanoparticle array. This data was used to analyze the average peak to valley height of the NPs, which is a useful measure of the average height of the particles. (b) AFM of the Ag NP array shown in (a) but after its heating in air at 100ºC for 100 minutes.*

Chapter 4

Conclusions

4.1 Summary

This thesis gives insight into the field of plasmonics and the potential novel nanostructures that can be created for sensing applications in the medical field as well as for magneto-plasmonics. One huge challenge for LSPR sensing, is finding a material that can yield high quality plasmons, is cost-effective, and is long-lasting. Literature can be found throughout that supports the usefulness of Ag over other metals, due to its high quality plasmon [12]. The drawback of Ag has been its susceptibility to oxidation. In this dissertation, the addition of Co to Ag and the resulting bimetallic nanoparticles were investigated. It should be mentioned here that during the course of this Master's level dissertation, one of my collaborators performed his PhD dissertation that overlapped with this work. The primary focus of his work was the synthesis of the materials, their structural characterization, and the TEM EELS study of the near-field behavior of the plasmonic properties of the bimetallic particles. The synthesis of nanoparticle arrays was performed by our collaborators using a pulsed laser dewetting technique developed by our group in which bi-layer films are first deposited and subsequently irradiated by a pulsed laser [34]. While all the samples were prepared and provided by my collaborator, our focus was to primarily investigate the plasmonic properties as well as potential for use of these materials in LSPR sensing applications.

The optical properties of pure Ag nanoparticle arrays were compared to that of AgCo nanoparticle arrays of various composition (72%Ag-28%Co and 83%Ag-17%Co) and average particle size (70 to 110 nm). The optical properties of Ag and the AgCo were studied using an HR 2000+ spectrometer from Ocean Optics in the transmission mode. The key results partly emphasized the advantage of tunability in wavelength of the AgCo over Ag, which is potentially useful for multiple applications. In our case, the plasmon frequency of AgCo could be tuned by ~200 nm by changing the particle diameter and Ag % composition. In contrast, Ag had a tunability of only about 20 nm. The bandwidth was evaluated with change in particle size and Ag % composition. As Co was added to Ag, the bandwidths increased on average. Within each Ag % composition, however, as the particle size increased, the LSPR red shifted with an increase in bandwidth. This followed the same trend reported in Link and El-Sayed's study for Au particles [10]. The sensitivity of the Ag and AgCo samples were studied through LSPR sensing by submerging these samples in different liquids: air (used as control), water, isopropanol, and glycerol. The important observation here was the high

sensitivity of AgCo. This had a similar or higher sensitivity than Ag for both the AgCo particle compositions investigated, where the average S value for Ag was 60 nm/RIU while that for AgCo ranged between 50 to ~100 nm/RIU. This result indicates that although Co is being added to Ag, the plasmon is not degrading, but improving. Ag being the material with better plasmonic properties, greatly contributes to the plasmon and if the plasmon is strong, this means something is happening in the structure that prevents this degradation. During these studies it was found that the Co is shielding the Ag from oxidation thus extending the plasmon lifetime and quality of the plasmon more so than pure Ag.

Oxidation studies were then performed on a newly synthesized batch of Ag and AgCo samples. Our collaborators performed oxidation studies by storage for long times in ambient air and the optical and LSPR sensitivity behavior was analyzed here. In addition, samples were also annealed at various temperatures up to 150°C for 100 minutes. The oxidation stability hypothesis for AgCo was confirmed for an 83%Ag-17%Co sample in comparison to pure Ag samples. AgCo was found to be stable and the plasmon wavelength and intensity (quality) was relatively constant throughout, as opposed to Ag which degraded quite rapidly. Sensitivity measurements were also carried out in these experiments, and provide further evidence that the AgCo was extremely stable as compared to pure Ag.

It is clear from the results of this work that AgCo can be a highly useful and advantageous material due to its tuning capabilities and sensitivity. The cost of adding Co to Ag is also not so expensive, considering Co is an inexpensive material. The main advantage of this system would be the resistance of AgCo to oxidation.

4.2 Future work

Based on the limited scope of this Master's thesis research, there are necessarily several threads to pursue to understand some of the findings in a broader manner. Here we highlight some of the more important ones.

1. It has been shown by Wang and co-workers [46] that the temporal rate of SPR sensing measurements can be enhanced by magnetic fields to guide superparamagnetically tagged molecules to the SPR metal surface . Our AgCo systems offers an in-site magnetic field due to the ferromagnetic state of the Co, as evidenced by our co-workers. Therefore, future studies on how the AgCo particles can also enhance LSPR rates could be of potential relevance to applications.

2. As presented in the discussion chapter, the AgCo system shows similar or enhanced sensitivity as compared to pure Ag. Since the LSPR sensitivity is strongly linked to the decay of the plasmon from the particle surface, an near field investigation of the localized surface plasmons in AgCo would be of fundamental importance in revealing why AgCo could be much better then Ag. In fact, this research is being pursued by my collaborators by using EELS measurements in the TEM.

Bibliography

[1] M. A. Garcia. Surface plasmons in metallic nanoparticles: fundamentals and applications. *Journal of Physics D: Applied Physics*, 44(28):283001, 2011.

[2] E. Petryayeva and U.J. Krull. Localized surface plasmon resonance: Nanostructures, bioassays and biosensing: A review. *Analytica Chimica Acta*, 706(1):8 – 24, 2011.

[3] K. A. Willets and R. P. Van Duyne. Localized surface plasmon resonance spectroscopy and sensing. *Annual Review of Physical Chemistry*, 58(1):267–297, 2007. PMID: 17067281.

[4] S.A. Maier. *Plasmonics: Fundamentals and applications*. Springer, New York, 2007.

[5] E. Hutter and J.H. Fendler. Exploitation of localized surface plasmon resonance. *Advanced Materials*, 16(19):1685–1706, 2004.

[6] K. M. Mayer and J. H. Hafner. Localized surface plasmon resonance sensors. *Chemical Reviews*, 111(6):3828–3857, 2011.

[7] T. Wriedt. Mie theory: A review. In Wolfram Hergert and Thomas Wriedt, editors, *The Mie Theory*, volume 169 of *Springer Series in Optical Sciences*, pages 53–71. Springer Berlin Heidelberg, 2012.

[8] G. Mie. *Ann. Phys (Leipzig)*, 25:377, 1908.

[9] M. A. Link, S.and El-Sayed. Shape and size dependence of radiative, non-radiative and photothermal properties of gold nanocrystals. *International Reviews in Physical Chemistry*, 19(3):409–453, 2000.

[10] S. Link, Z.L. Wang, and M.A. El-Sayed. Alloy formation of gold-silver nanoparticles and the dependence of the plasmon absorption on their composition. *Journal of Physical Chemistry B*, 103(18):3529–3533, 1999.

[11] M.G. Blaber, M.D. Arnold, and M.J. Ford. A review of the optical properties of alloys and intermetallics for plasmonics. *Journal of Physics: Condensed Matter*, 22(14):143201, 2010.

[12] P.R. West, S. Ishii, G.V. Naik, N.K. Emani, V.M. Shalaev, and A. Boltasseva. Searching for better plasmonic materials. *Laser & Photonics Reviews*, 4(6):795–808, 2010.

[13] U. Kreibig. Limitation of electron mean free path in small silver particles. *European physical journal*, 224:307, 1969.

[14] E. J. Heilweil and R. M. Hochstrasser. Nonlinear spectroscopy and picosecond transient grating study of colloidal gold. *The Journal of Chemical Physics*, 82(11):4762–4770, 1985.

[15] A. Wei. Plasmonic nanomaterials. In Vincent Rotello, editor, *Nanoparticles*, Nanostructure Science and Technology, pages 173–200. Springer US, 2004.

[16] H. Garcia and R. Kalyanaraman. Internal communication. 2012.

[17] L. Novotny and B. Hecht. *Principles of Nano-Optics*. Cambridge University Press, Cambridge, 2006.

[18] N.I. Kulikov and E.T. Kulatov. Electronic band structure, fermi surface and optical properties of cobalt under pressure. *J . Phys. F: Met. Phys.*, 12:2267–89, 1982.

[19] H. Garcia and R. Kalyanaraman. Theoretical optical absorption of ag vs co nanoparticles. *unpublished*, 2012.

[20] J. N. Anker, W. P. Hall, O. Lyandres, N. C. Shah, J. Zhao, and R. P. Van Duyne. Biosensing with plasmonic nanosensors. *Nature Materials*, 7(6):442–453, 2008. Anker, Jeffrey N. Hall, W. Paige Lyandres, Olga Shah, Nilam C. Zhao, Jing Van Duyne, Richard P.

[21] A.N Grigorenko, H.F. Gleeson, and Y. Zhang. Antisymmetric plasmon resonance in coupled gold nanoparticles as a sensitive tool for detection of local index of refraction. *Appl. Phys. Lett.*, 88:124103, 6.

[22] M. Zayats, S.P. Pogorelova, A.B. Kharitonov, O. Lioubashevski, E. Katz, and I. Willner. An nanoparticle-enhanced surface plasmon resonance sensing of biocatalytic transformations. *Chemistry-A European Journal*, 9(24):6108–6114, 2003.

[23] B. Sepúlveda, A. Calle, L. M. Lechuga, and G. Armelles. Highly sensitive detection of biomolecules with the magneto-optic surface-plasmon-resonance sensor. *Opt. Lett.*, 31:1085, 2006.

[24] Jack J. Mock, David R. Smith, and Sheldon Schultz. Local refractive index dependence of plasmon resonance spectra from individual nanoparticles. *Nano Letters*, 3(4):485–491, 2003.

[25] LamdaGen Corporation. Lamdagen lspr biosensor chips compared to gold colloids.

[26] T. E. Graedel. Corrosion mechanisms for silver exposed to the atmosphere. *Journal of The Electrochemical Society*, 139(7):1963–1970, 1992.

[27] Y. Yin, Z.-Y. Li, Gates B. Xia Y. Zhong, Z., and S. Venkateswaran. Synthesis and characterization of stable aqueous dispersions of silver nanoparticles through the tollens process. *J. Mater. Chem.*, 12:522–527, 2002.

[28] J. Lakowicz C. Geddes K. Aslan, Z. Leonenko. Annealed silver-island films for applications in metal-enhanced fluorescence: Interpretation in terms of radiating plasmons. *Journal of Fluorescence*, 15:643–654, 2005.

[29] J. Sippel-Oakley Y. Choi and A. Ural. Single-walled carbon nanotube growth from ion implanted fe catalyst. *Appl. Phys. Lett.*, 89(15):153130, 2006.

[30] R. Cao and C.A. Mirkin. Dna-modified core shell ag/au nanoparticles. *Journal of the American Chemical Society*, 123(32):7961–7962, 2001.

[31] P. Singh K. Higashimine D.M. Mott C. Shankar, A.T.N. Dao and S. Maenosono. Chemical stabilization of gold coated by silver core shell nanoparticles via electron transfer. *Nanotechnology*, 23(24):245704, 2012.

[32] C. C. Tyson, A. Bzowski, P. Kristof, M. Kuhn, R. Sammynaiken, and T. K. Sham. Charge redistribution in au-ag alloys from a local perspective. *Phys. Rev. B*, 45:8924–8928, 1992.

[33] S. Yadavali M. Khenner and R. Kalyanaraman. Formation of organized nanostructures from unstable bilayers of thin metallic liquids. *Physics of Fluids*, 23(12):122105, 2011.

[34] R. Sachan, S. Yadavali, N. Shirato, H. Krishna, V. Ramos, G. Duscher, S. J. Pennycook, A. K. Gangopadhyay, H. Garcia, and R. Kalyanaraman. Self-organized bimetallic Ag-Co nanoparticles with tunable localized surface plasmons showing high environmental stability and sensitivity. *Nanotechnology*, 23(27):275604, 2012.

[35] H. Garcia, R. Kalyanaraman, and R. Sureshkumar. Nonlinear optical properties of multi-metal nanocomposites in a glass matrix. *J. Phys. B: Atomic, Molecular and Optical Physics*, 42(17):175401, 2009.

[36] H. Garcia, J. Trice, R. Kalyanaraman, and R. Sureshkumar. Self consistent determination of plasmonic resonance in ternary nanocomposites. *Phys. Rev. B*, 75:045439–1–4, 2007.

[37] C. Sönnichsen, T. Franzl, T. Wilk, G. von Plessen, J. Feldmann, O. Wilson, and P. Mulvaney. Drastic reduction of plasmon damping in gold nanorods. *Phys. Rev. Lett.*, 88(7):077402, 2002.

[38] U. Kreibig and M. Vollmer. *Optical Properties of Metal Clusters*. Springer, Berlin, 1995.

[39] H. Krishna, J. Strader, A. K. Gangopadhyay, and R. Kalyanaraman. Nanosecond laser-induced synthesis of nanoparticles with tailorable magnetic anisotropy. *J. Mag. Mag. Mat.*, 323:356–362, 2011.

[40] R. Sachan. *Novel Bimetallic Plasmonic Nanomaterials*. PhD thesis, The University of Tennesse-Knoxville, 2012.

[41] Yun Han, Robert Lupitskyy, Tseng-Ming Chou, Christopher M. Stafford, Henry Du, and Svetlana Sukhishvili. Effect of oxidation on surface-enhanced raman scattering activity of silver nanoparticles: A quantitative correlation. *Analytical Chemistry*, 83(15):5873–5880, 2011.

[42] R. Sachan et.al. Oxidation- resistant ag nanostructures for ultrastable plasmoninc applications. *Unpublished*, 2012.

[43] H. G. Tompkins and J. A. Augis. The oxidation of cobalt in air from room temperature to 467 c. *Oxidation of Metals*, 16:355, 1981.

[44] M. G. Fontana. *Corrosion engineering*. McGraw-Hill, New York, internattional edition, 1987.

[45] D. Linde, editor. *The CRC Handbook of Chemistry and Physics*. CRC Press, Boca Raton, 1992.

[46] Y. Wang, J. Dosalek, and W. Knoll. Magnetic nanoparticle-enhanced SPR biosensor. *Procedia Eng.*, 5:1017–1020, 2010.

Vita

Vanessa Ramos was born in New Brunswick, New Jersey on February 11, 1986. She graduated from The University of Tennessee, Knoxville in May 2010 with a Bachelor of Science degree in Biomedical Engineering. In December 2012, she completed her Master of Science degree in Materials Science and Engineering.